The Development and Evaluation of the Experimental Gravimetric Geoid Model 2019

Xiaopeng Li, Kevin Ahlgren, Ryan Hardy, Jordan Krcmaric, and Yan Ming Wang

1. Introduction

In 2014, the United States National Geodetic Survey (NGS) started producing annual experimental gravimetric geoid models, the xGEOID models, for the upcoming vertical datum modernization in 2022, the North American-Pacific Geopotential Datum of 2022 (NAPGD2022). At the beginning of each year, two types of gravimetric geoid models are built using the latest data, models, and techniques. The type A model is computed without including the GRAV-D airborne gravity data. Keeping everything else the same, the type B model is computed by adding all of the available GRAV-D airborne gravity data. The GRAV-D effects on the geoid model can be easily obtained by differencing the B model with the A model.

The xGEOID19 model covers the entire region of North America, including the continental United States (CONUS), the states of Alaska and Hawaii, the U.S. territories of Puerto Rico and the U.S. Virgin Islands, and neighboring countries such as Canada and Mexico. The exact geographic extent of the area is from latitude 85^{o}N to the equator in the north-south direction, and from longitude 170^{o}E to longitude 350^{o}E in the east-west direction. xGEOID19 is based on a 1'x1' gravity grid and a seamless 3''x3'' digital elevation model (DEM) derived from the North American common gravity and DEM database that has recently been compiled by NGS (Ahlgren, et al., 2018). The xGEOID19 model is computed from the xGEOID16RefA coefficient model, which is a combination of EGM2008 and GOCO05s up to degree and order 2160.

This document provides a detailed description of the development and evaluation of the xGEOID19 model. The data usage, modeling method, and evaluation techniques will be extensively discussed in order to provide useful and manageable guidelines for further geoid model improvements.

The rest of the report is organized as follows. In section 2, a detailed description of analyzing, merging and integrating surface gravity data sets from various agencies such as NGS, NRCan, and NGA will be given. This newly built common gravity dataset serves as the foundation for the future vertical datum unification between the U.S., Canada, and Mexico. Section 3 describes the key steps of generating a seamless 3''x3'' DEM over North America. Section 4 contains the explicit formulas for the xGEOID19A computation and details of the intermediate results as well as the final xGEOID19A model. Section 5 is focused on GRAV-D airborne gravity modeling, downward continuation tests, xGEOID19B generating strategies, and the final xGEOID19B model. Model evaluation is given in section 6, where classical GPS/leveling, astronomical deflections of the vertical, and satellite altimetry are used to validate the final xGEOID19 model. Finally, section 7 contains a discussion and summary that will highlight the improvements and problems in the xGEOID19 model.

2. Input Datasets and Their Combination

Terrestrial Gravity Data:

xGEOID19 makes use of a newly merged gravity dataset that is different from previous xGEOID models computed at NGS. This dataset is made up of five components: terrestrial gravity data, airborne gravity data, altimetric gravity data, a satellite gravity model, and a DEM.

The terrestrial surface gravity data is a combination of gravity data from NGS, NGA, NRCan, and DTU. Each geographic region is handled slightly differently due to idiosyncrasies with the dataset(s). As an example within CONUS, the NGA data is added to the database first, then any residual NGS data that has a unique location (latitude, longitude, orthometric height) is added to supplement the NGA data. Over Canadian areas, NRCan data is used exclusively. The database contains 1,650,169 gravity points used in this xGEOID model. The data density is shown in Figure 1.

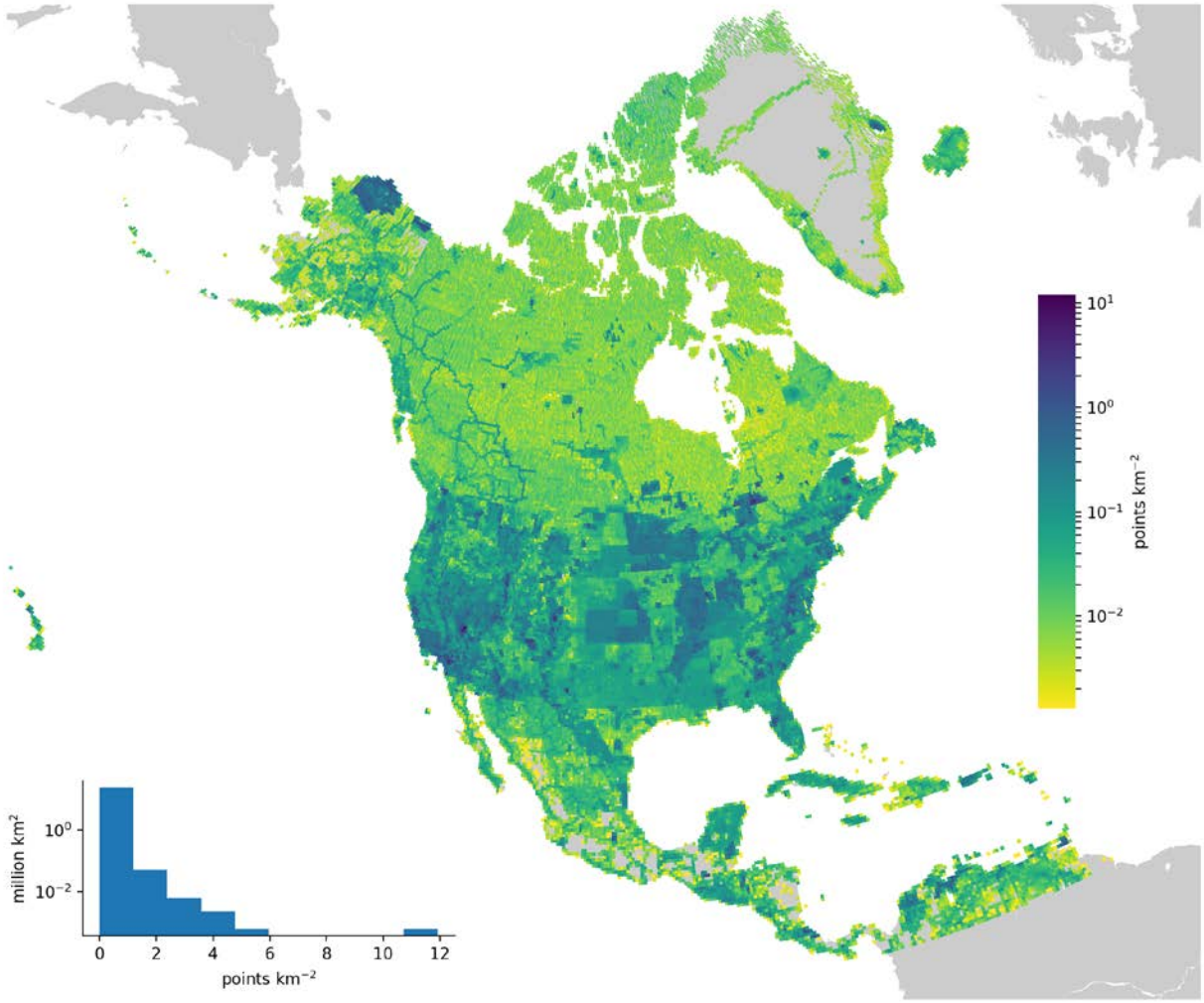

Figure 1. Terrestrial gravity anomalies used in xGEOID19.

The totals are broken down into separate geographic regions and are listed in Table 1.

Table 1: Input Gravity data to North American common gravity dataset.

	Geographic Region:	Total Number of Points:	Comments:
1	CONUS, Hawaii, Alaska excluding the Great Lakes	1,222,973	NGA data (1,138,596) / NGS data (84,377)
2	Lake Huron, Lake Ontario, and Lake Superior	17,563	NGA data (17,543) / NGS data (20)
3	Lake Michigan	3,151	Data has been cleaned due to known issues (Li, et al., 2016)
4	Canada and Lake Erie	251,313	NRCan-CGS data
5	Caribbean Islands	18,373	NGA data
6	Mexico and Central America	106,210	NGA data
7	South America	15,121	Supplemental data from 7 – 10 degrees from NGS
8	Greenland and Iceland	15,465	DTU data

The free-air anomalies and simple Bouguer anomalies are computed for all of the surface gravity data according to NGA, 2008 and depend on the specific observation type (e.g., surface, below-surface, on ice-cap, lake-surface, lake-bottom, and airborne).

Previous geoid modeling results identified a problem with the data in Lake Michigan (Li et al., 2016). As such, the 3,151 data points in Lake Michigan have been cleaned for xGEOID19 using a satellite-only gravity model to estimate and correct long-wavelength features in the surface data.

In addition, 251,313 data points throughout Canada and Lake Erie are provided by NRCan. The decision to use Canada's data in Lake Erie is based on evidence that previous NRCan geoid models fit much better than NGS geoid models around Lake Erie when compared with water gauge stations (Marc Veronneau, personal communication).

Gravity data sources are shown in Figures 2 (full extent) and 3 (CONUS only).

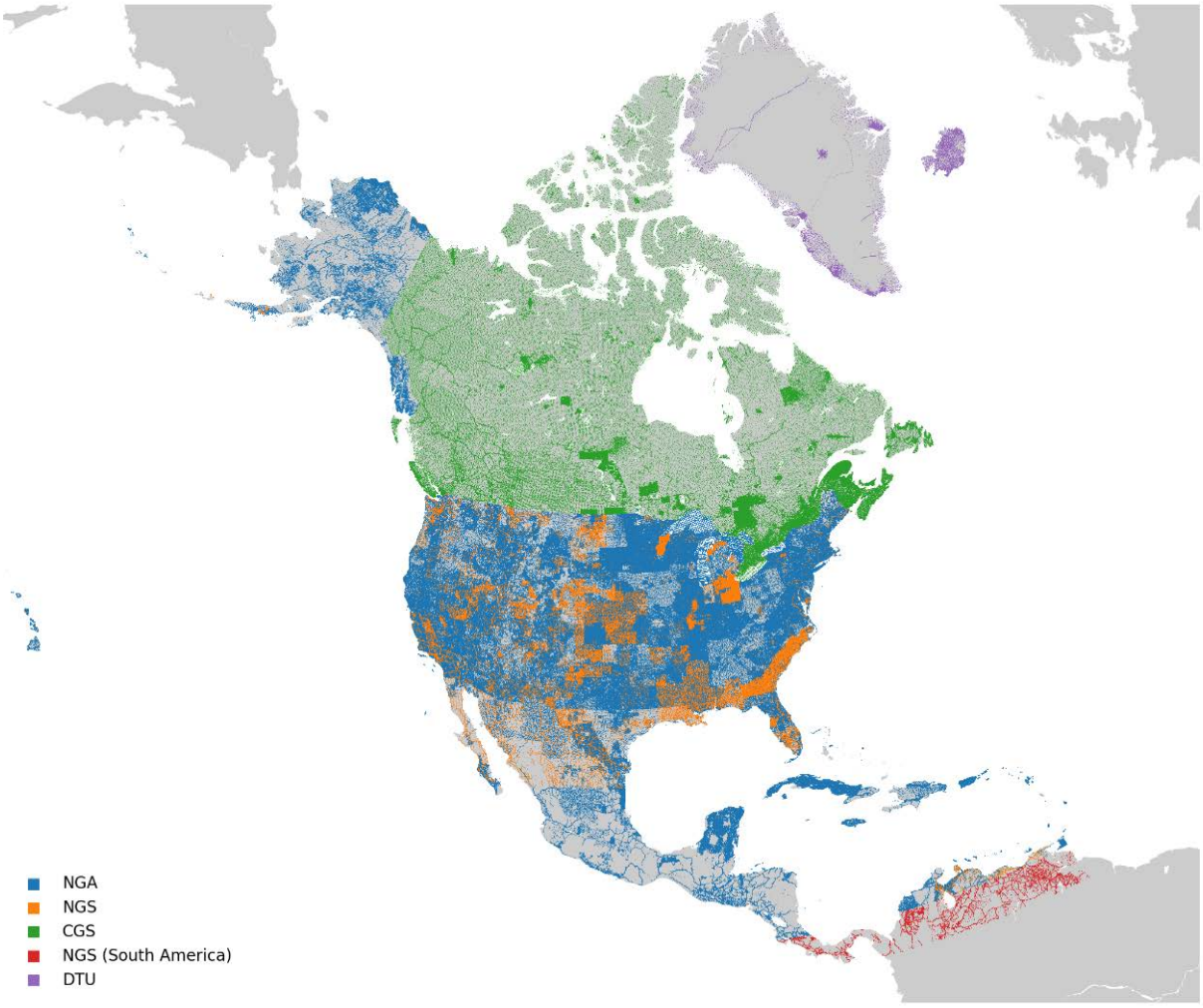

Figure 2. Surface gravity data with source agency.

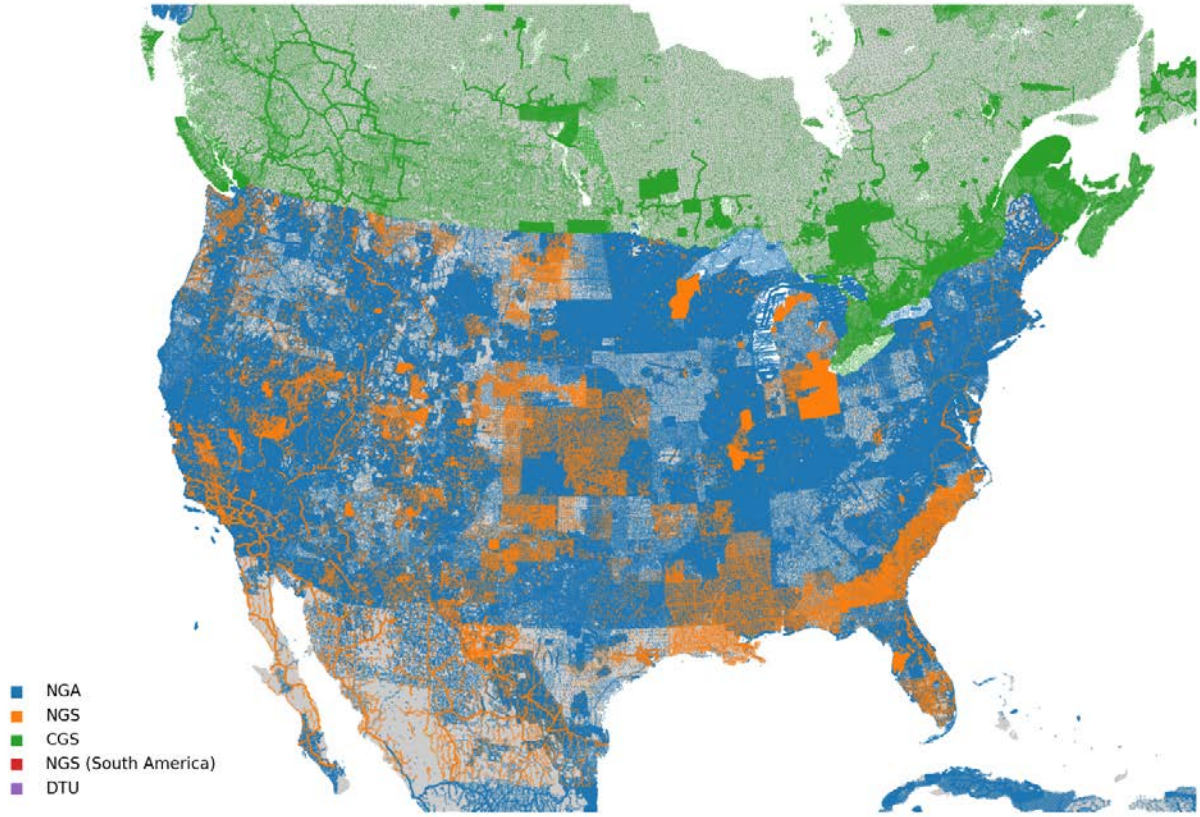

Figure 3. Terrestrial gravity data sources within CONUS.

Altimetric Gravity Data:

Gravity data over the ocean areas are based on the DTU15 model (Andersen et al. 2016). These anomalies are provided with respect to the TOPEX/Poseidon ellipsoid, which is converted to the GRS80 ellipsoid by adding the difference of the normal gravity between the reference ellipsoids (latitude dependent) term: $\gamma_{TP} - \gamma_{GRS80}$

The gravity anomalies are shown in Figure 4.

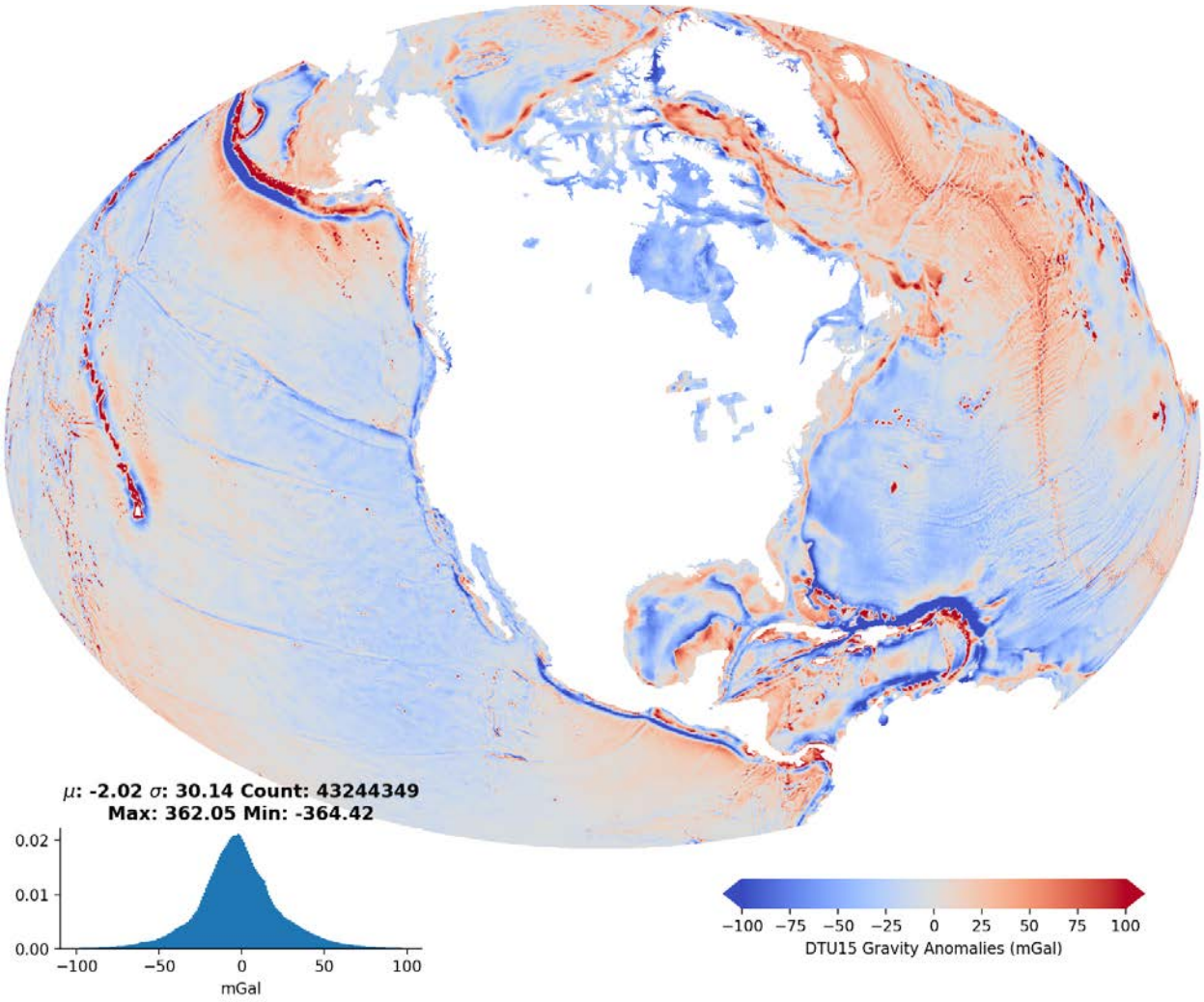

Figure 4: DTU15 gravity anomalies over the open seas around the modeling area.

GRAV-D Airborne Data:

The publically available GRAV-D data are obtained directly from the NGS website (https://www.ngs.noaa.gov/GRAV-D/data_products.shtml). For each of the blocks used, an individual survey line bias is estimated and removed based on the median difference from the xGEOID16RefA model. The 53 blocks that were used in xGEOID19B model development are listed in Appendix I. New blocks since xGEOID18B (15 total) include AN09, AS05, AS07, CN01, CN04, CN05, CS08, ES06, ES09, ES10, MS03, MS04, MS05, PN02, and PS02.

3. DEM Generation

SRTMv4.1 (Jarvis et al., 2008) is used for all areas south of 60°N. Models used north of 60°N include ASTER for the state of Alaska (Li et al., 2008), CDED for the Canadian regions (Huang and Véronneau, 2013), GIMPv1 (Howat et al., 2014) for Greenland, and MERIT (Yamazaki et al., 2017) for Iceland.

A minor amount of processing is performed on the DEM. First, a despiking procedure is performed on the DEM that flags immediately neighboring cells that have a 500 m difference and then fixes the incorrect cells. Secondly, the DEM requires some patching in a small number of mountainous areas. To remedy these areas, a 2 km radius surrounding all the incorrect cells is extracted, all the incorrect cell values are removed, and then a biharmonic spline interpolation is used to fill the incorrect cells (Ahlgren et al., 2018). The patching process is shown in Figure 5.

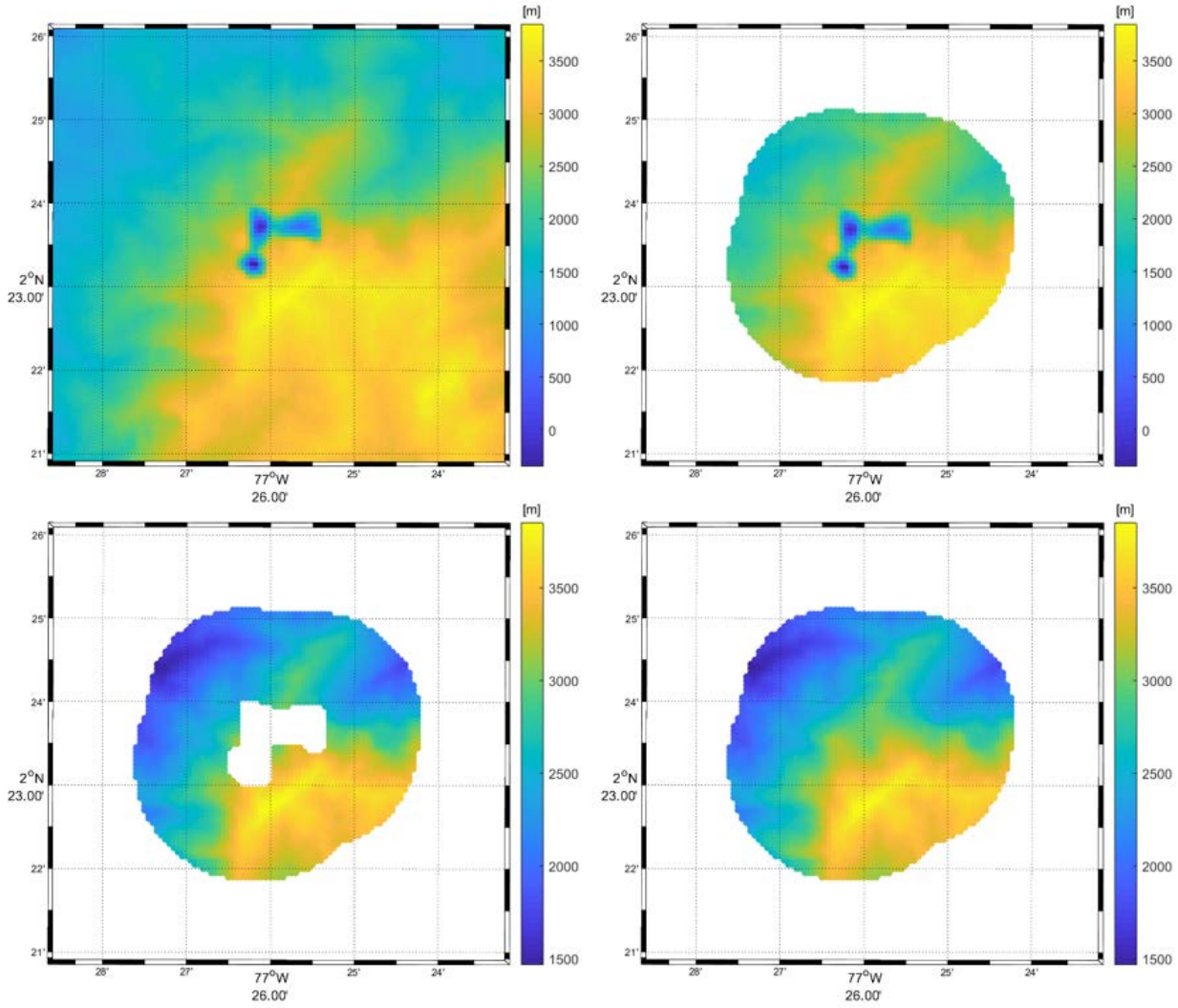

Figure 5: Detected artifacts and the corresponding fixing result in the area of 2°N, 77°W from Ahlgren, et al., 2018. Original DEM (top left), 2 km buffer (top right), Extraction of cells to fill (lower left), Biharmonic Spline Interpolation (lower right).

4. Type A Geoid Modeling Procedure and Results

The xGEOID19A model is computed by using exactly the same technique as used in the USGG2009 model (Wang et al., 2012). xGEOID16RefA is used as the reference model for xGEOID19 computations because it was discovered to perform much better in the state of Colorado compared to the xGEOID17RefA model.

For the reader's convenience, as well as for self-consistency and providing a context for the following discussions, xGEOID19A is computed as follows:

$$N = \frac{R}{4\pi\gamma}\iint_{\sigma}\delta\Delta g S^{M}(\psi)d\sigma + \zeta^{REF}_{2\rightarrow 2160} + \zeta^{RTM}_{2161\rightarrow 3''} + \Delta N \quad (1)$$

with

$$\delta\Delta g = \Delta g^{OBS} + \Delta g^{ATM} - \Delta g^{REF}_{2\rightarrow 2160} - \Delta g^{RTM}_{2161\rightarrow 3''}$$

where Δg^{OBS} is the observed gravity anomalies that is described in Section 2; Δg^{ATM} and $\Delta g^{REF}_{2\rightarrow 2160}$ are the atmospheric correction and the synthesized gravity anomalies from xGEOID16RefA at the same location as the observation point, respectively; $\Delta g^{RTM}_{2161\rightarrow 3''}$ is the residual terrain effects (Forsberg 1984); $S^{M}(\psi)$ is the modified Stokes' integration function; $\zeta^{REF}_{2\rightarrow 2160}$ and $\zeta^{RTM}_{2161\rightarrow 3''}$ are the corresponding restore terms from the reference model and the residual terrain, respectively; and ΔN is the classical geoid-quasigeoid separation term, which will be further discussed in Section 7.

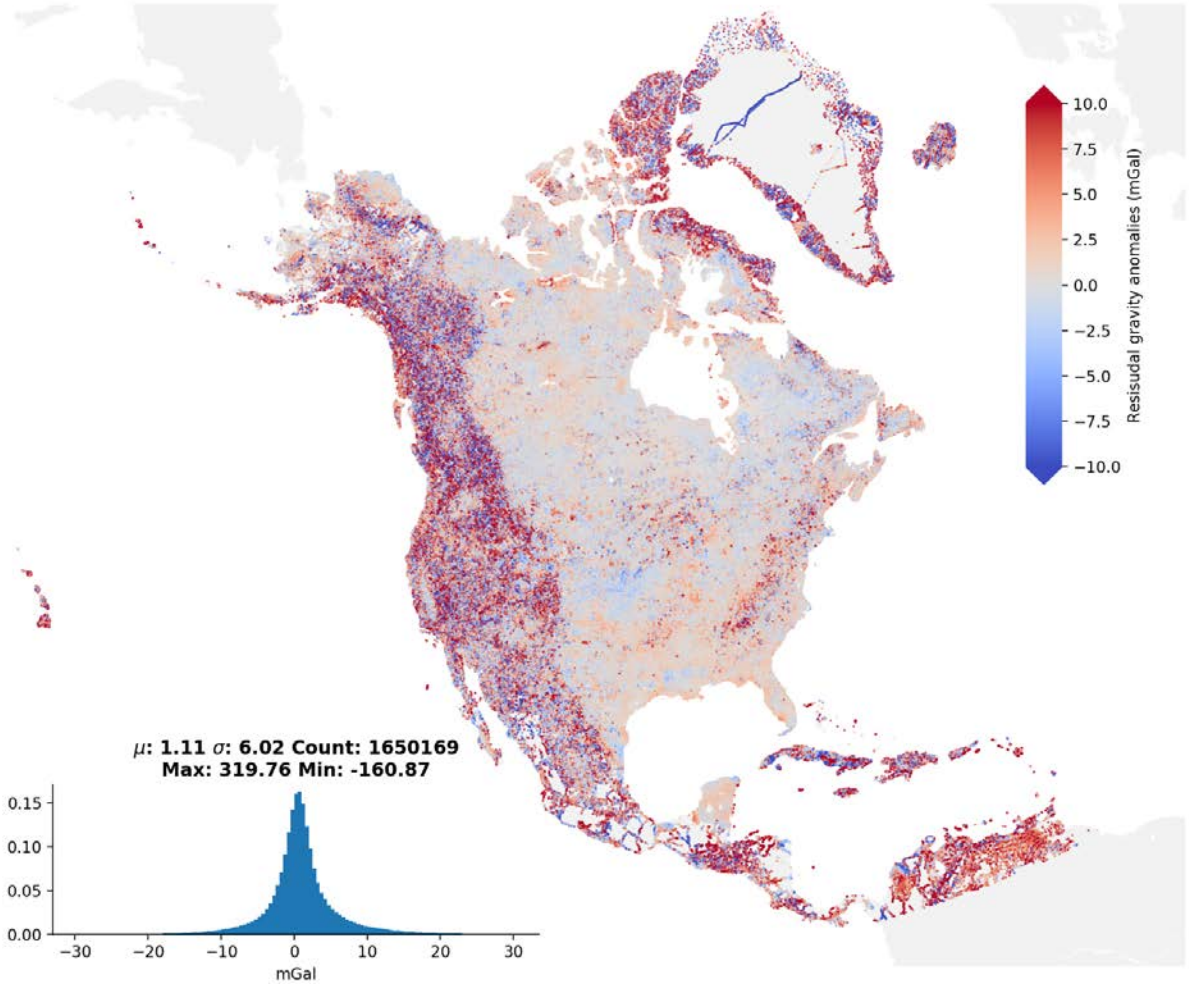

Figure 6: Residual gravity anomalies in the land area.

Figure 6 shows the residual gravity anomalies before gridding and feeding into Eq. (1). The statistics of the original data, each reduction term, and the final residuals are summarized in Table 2.

Table 2 shows that there is a -1.9 mGal bias in the terrestrial data after removing the reference field to degree and order 2160. Comparing the last 2 rows in Table 2 shows that the RTM procedure reduces the power of the higher frequencies in the gravity data. The standard deviation is decreased from 11 mGal to 6 mGal. However, it also introduces a ~3 mGal bias. Because a modified Stokes' kernel (Wong and Gore, 1969) is used, the biases in the gravity data will be filtered out.

After adding back the reference model and RTM effect on the geoid, the final xGEOID19A is computed. Figure 7 shows the residual geoid which contains most its power in the higher frequencies of the gravity field. The larger signal is strongly correlated with topography.

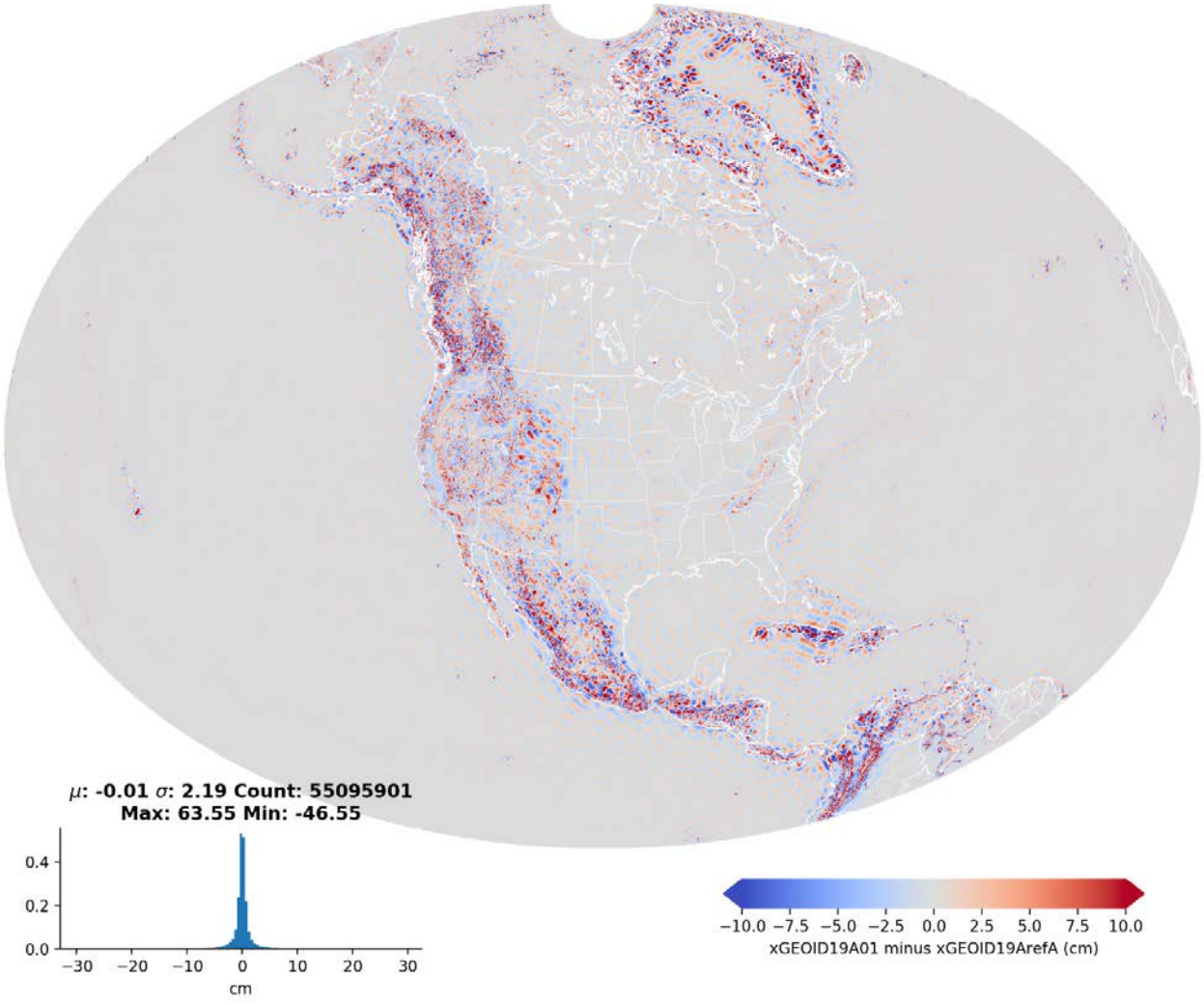

Figure 7: The local gravity and topographic contribution to xGEOID19A.

5. Type B Geoid Modeling Procedure and Results

NGS combines the gravity data using the Spherical Harmonic Analysis (SHA) method (Smith et al., 2013), which is described in the following paragraphs.

After removing the xGEOID16RefA reference field, T^{ref}, and terrain effects, T^{RTM}, from the debiased GRAV-D gravity data, the residual gravity disturbances are filtered and averaged to 1 km along-track resolution. The residual airborne gravity disturbances (δg^{res}) can be expressed by a series of spherical harmonics as follows:

$$\delta g^{res}(r, \phi \ \ , \lambda \ \ ) \approx -\frac{\partial \delta T}{\partial r}$$

$$= \frac{GM}{R^2} \sum_{n=n1}^{n2} \left(\frac{R}{r}\right)^{n+2} (n+1) \sum_{m=0}^{n} \left(\underline{c}_{nm}^{\delta T} cos\,(m\lambda) \ + \underline{s}_{nm}^{\delta T} sin\,(m\lambda) \right) \underline{p}_{nm}(sin\phi) \qquad (2)$$

where $\delta T = T \ \ - T^{ref} - T^{RTM}$ is the residual gravity disturbing potential after removing a reference field and terrain effects; GM is the geocentric gravitational constant; R is the mean radius of Earth; $\underline{p}_{nm}$ are the fully normalized associated Legendre functions of degree n and order m; $\{\underline{c}_{nm}^{\delta T}, \underline{s}_{nm}^{\delta T}\}$ are the Stokes's coefficients to be solved from the reduced airborne gravity anomalies $\delta g^{res} = \delta g^{airborne} - \delta g^{ref} - \Delta g^{RTM}$; and $n1$ and $n2$ are the primary spectrum band of the gravity data, which can be estimated from the data by various methods (ibid).

Solving for $\{\underline{c}_{nm}^{\delta T}, \underline{s}_{nm}^{\delta T}\}$ presents a challenge. Since airborne gravity surveys are carried out in local areas, and not global in extent, there is not enough data to solve the inverse problem. Thus, the residual field outside of the airborne survey region is set to zero. In other words, the gravity value of the reference model is used in the areas outside the survey region to satisfy the requirement for global data coverage.

The GRAV-D data has been collected at varying flight altitudes, so it needs to be reduced to an expanded ellipsoid (with the same eccentricity as GRS80, but semi-major axes $a \ = \ a_{GRS80} + \bar{h}$, where $\bar{h}$ is the mean flight altitude of the survey). Then the residual coefficients $\{\underline{c}_{nm}^{\delta T}, \underline{s}_{nm}^{\delta T}\}$ of the survey are computed using the same method as EGM2008 (Pavlis et al., 2012).

The power is mainly concentrated from degree 200 to degree 800 in the spectrum domain, except when there is heavy leakage to the low degree terms after the above SHA process. As such $\{W_n^{GRAV-D}\}$ is designed to only include terms from degree 200 to 800, giving the optimal band a weight of 1 and gradually tapering to zero. Surface gravity data and NAVD88 leveling benchmarks free of systematic errors (Li et al., 2018a) are also used to fine-tune the weight parameters. These procedures are applied individually to each of the 53 blocks so that all of the GRAV-D data can be harmonically downward continued onto the reference ellipsoid. Finally, an ensemble SHA is performed on the harmonic downward continued residual GRAV-D gravity data. To reduce the edge effects of the isolated blocks, a 200 km tapering function is applied.

The fine-tuning procedure resulted in 11 global coefficient models being developed. The models are validated against independent data sets, namely the historical GPS/leveling data,

mean lake surface height over the Great Lakes, and the Geoid Slope Validation Surveys of 2011 (GSVS11; Smith et al., 2013) and 2014 (GSVS14; Wang et al. 2017). Evaluation of the coefficient models determined the best performing model to be xGEOID19RefB11, which was selected to serve as the final reference model, xGEOID19RefB.

The final GRAV-D airborne gravity effects on the geoid for the xGEOID19B model are shown in Figure 8.

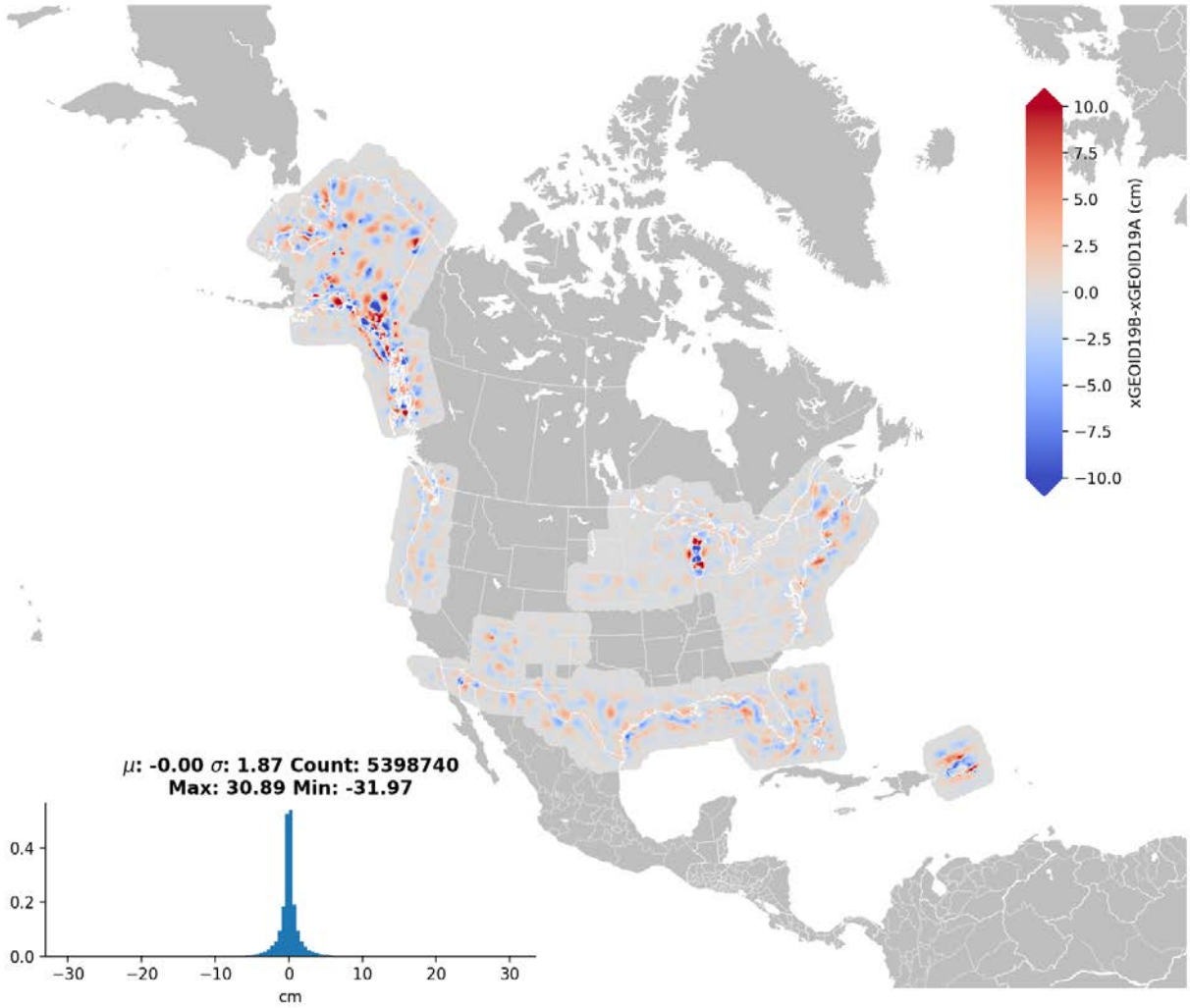

Figure 8. Effects of GRAV-D airborne gravity data on xGEOID19.

Geoid changes from GRAV-D exceed ±30 cm in Alaska, especially in the southeast and southcentral regions. While much of this improvement can be attributed to GRAV-D overcoming the limits of terrestrial gravity coverage, the changes in southcentral and southeast Alaska are also largely reflective of time variations in the gravity field. In southern Alaska, a mix of present-day ice mass loss and solid-Earth processes drive geoid change exceeding 3 mm yr^{-1} and surface elevation change of more than 10 mm yr^{-1} (Jacob et al., 2012; Snay et al., 2016). More than 80% of terrestrial gravity measurements in Alaska were collected prior to 1980 (Barnes, 1976; Saltus

et al., 2008), whereas GRAV-D data reflect the state of the gravity field circa 2010. Peak accumulated geoid change across this interval is expected to approach 10 cm and surface uplift is expected to exceed 30 cm. Additionally, episodic elevation changes of 1–2 m during the 1964 Prince William Sound earthquake also contribute to time-dependent systematic gravity errors in Alaska applicable to data collected before this event. The coincidence of the strongest geoid change signals with the locations of mountain glaciers with the most intense mass loss provides strong circumstantial evidence for the mixture of time variation and signals of static geoid improvement. The nature of these errors may be confirmed by isolating differences between the pre-1980 terrestrial data and modern data. This provides an opportunity for direct measurement of geoid change. If confirmed, these errors may be rectified in future models with corrections to the terrestrial gravity data from a time-dependent gravity and elevation model.

In Lake Michigan, about 40 cm (peak to peak) geoid changes are seen due to the GRAV-D contribution. This change has been verified as geoid improvement (Li et al., 2016). Over Colorado where the Geoid Slope Validation Survey of 2017 (GSVS17) was conducted, GRAV-D contribution is not significant due to the good quality and distribution of the terrestrial gravity data in that region (Wang et al., 2019).

6. Evaluation

The developed models are evaluated mainly based on four categories of independent data. They are (1) historical GPS/leveling benchmarks, (2) averaged mean lake surface heights from over 20 years of multi-mission altimetry data (Berkeley et al. 2013), (3) historical measurements of deflections of the vertical, and recent inland water surface slope measurements from ICESat-2, and (4) the GSVS11 and GSVS14 comparisons.

(1) The historical GPS/leveling NAVD88 (Zilkoski and Young, 1992) benchmarks are used to evaluate the global coefficient models. To avoid the effect of density anomalies in the topography, the height anomalies computed on the GPS/leveling data are used to compare with the coefficient models. Figure 9 shows the precision of the reference models with and without GRAV-D data. From Figure 9, we see that the GRAV-D airborne gravity data improves the precision of the model in most states.

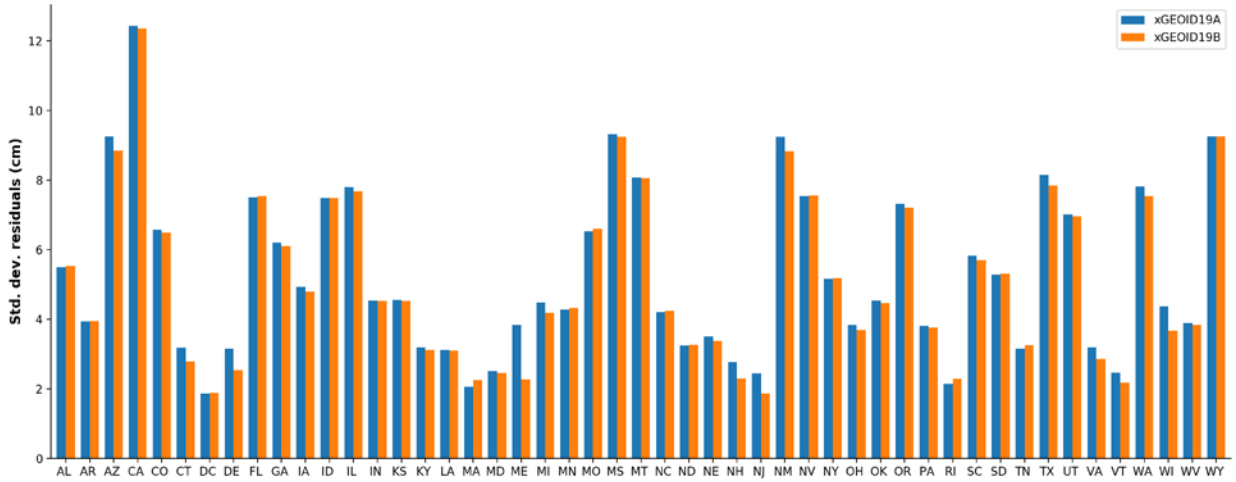

Figure 9. State-by-state height anomaly comparison of the developed reference models for xGEOID19 (with (B) and without (A) GRAV-D gravity data).

(2) Mean lake surface heights derived from multi-year multi-mission altimetry data (Li et al., 2016) is also used for evaluation. If we assume the mean lake surfaces are good approximations of equipotential surfaces, the dynamic heights of the mean lake surface heights along each pass should be a constant. Figure 10 shows the standard deviations of the dynamic heights along each pass over the Great Lakes. We see that the model precision is improved from the decimeter level to the 1-2 centimeter level after adding GRAV-D data in the Lake Michigan area. There are also minor improvements in the other Great Lakes.

Figure 10. The dynamic height variations computed from the models on the assumed constant heights over the Great Lakes.

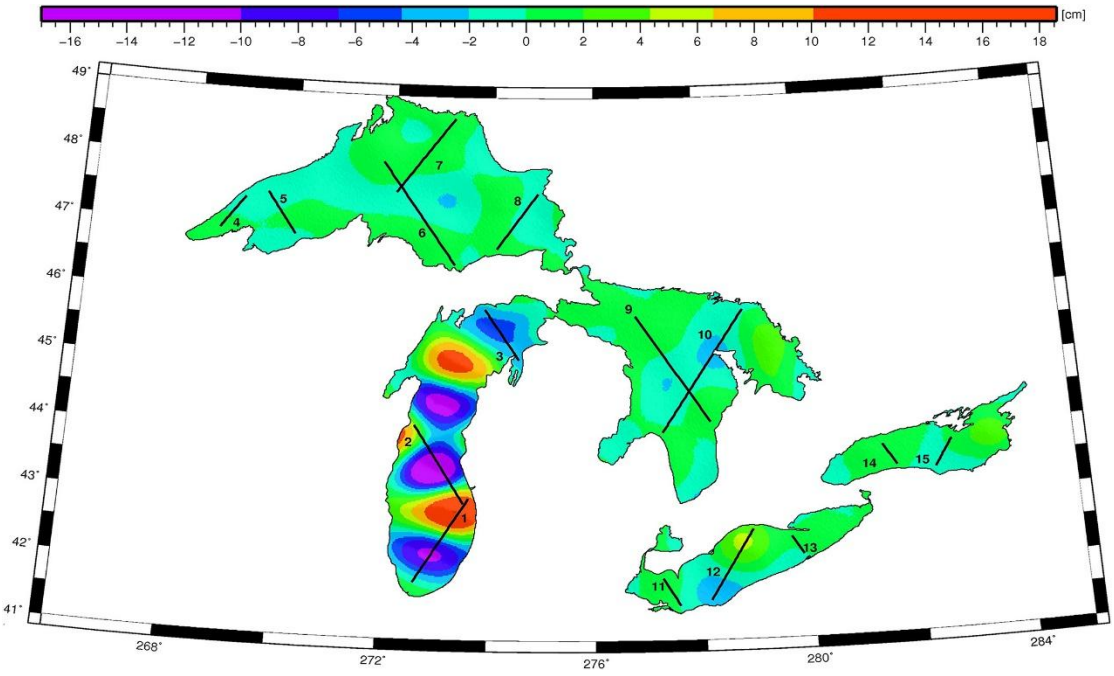

a) Location of the passes.

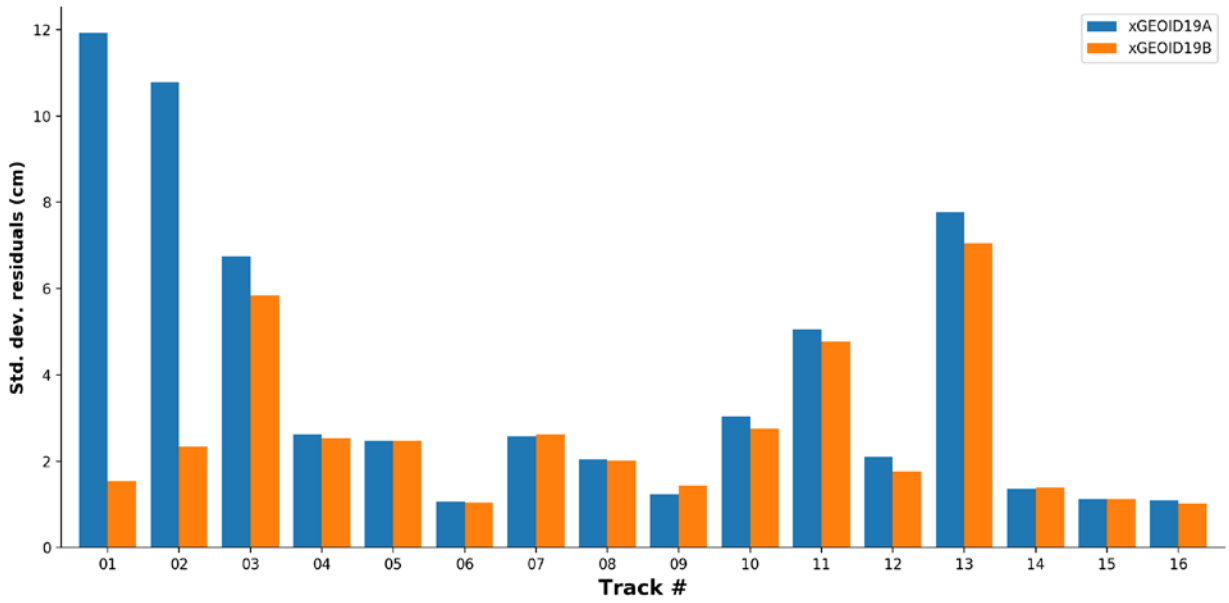

b) Precision comparisons before and after adding GRAV-D data.

(3) Deflections of the vertical and geoid slopes obtained from historical astronomical observations performed by NGS and the Coast & Geodetic Survey and recent inland water surface altimetry from ICESat-2. Astrogeodetic observations show 1.2” overall geoid slope precision over CONUS. States in the Eastern and Central time zones agree with astrogeodetic observations with 0.6” precision, while Pacific and Mountain states have 1.7” precision. Geoid slope precision in Alaska is 2.2”. Water surface slope measurements from ICESat-2 show statistically significant improvement in residuals over the Great Lakes. Details on the analysis of deflections of the vertical and altimetry-derived geoid slopes may be found in Appendix II.

(4) The GSVS11 and GSVS14 are two traverses over 300 km in length that cross eastern Texas and central Iowa, respectively. The traverses provide an independent dataset to test the accuracy of the geoid model in regions with different magnitudes of geoid slope and topographic variability. GPS/leveling, gravity and deflections of the vertical are collected along the traverses at a spacing of 1 mile. The GPS/leveling implied geoid heights are estimated to have 1 cm accuracy between the marks, and are used to compare against the xGEOID19A/B models. The results are shown in Table 3.

7. Summary and Discussion

A common gravity and DEM database for the U.S., Canada, and Mexico is compiled for the first time. This database provides excellent gravity coverage and a seamless high-resolution DEM in the target region. The xGEOID19A model is computed from this common database by using the xGEOID16RefA coefficient model as a reference model in the classical remove-compute-restore procedure. Airborne gravity from 53 GRAV-D data blocks is transformed into residual spherical harmonic coefficients by using the SHA method developed at NGS. These residual coefficients are combined with xGEOID16RefA using empirical weighting coefficients.

After 11 rounds of fine-tuning the model, a final coefficient model, xGEOID19RefB, is generated as a reference model for xGEOID19B. The precision of height anomalies on historical GPS/leveling benchmarks is improved in states where the GRAV-D airborne data is available. Up to 40 cm of improvement is also seen in Lake Michigan, as well as smaller improvements in the other Great Lakes, from comparisons to mean lake surface height measurements. Larger geoid changes due to GRAV-D data are found in the Alaska/Yukon area. The changes are a mixture of time-variable gravity and improvement in the static geoid. These changes need to be further investigated to separate the two effects. In addition, independent data sets from GSVS11 and GSVS14, and astronomical and ICESat-2-derived deflections of the vertical are also used to validate the xGEOID19 model. All of these tests show consistent geoid model improvement after adding the GRAV-D data.

However, during the course of model development, some problems also have been identified in the data preparation, modeling procedure, and model evaluation. For example, lake bottom gravity measurements will need to be correctly handled to keep consistency with the current NGS geoid modeling procedure. Numerous duplicate points with inconsistent gravity values were also identified in the common gravity dataset. These duplicate points will need to be further investigated to determine which gravity value is the correct one to include, since choosing different values can produce changes up to 1 cm in the geoid model (Krcmaric et al., 2019). Ship track gravity data and other altimetry products will also need to be incorporated for future geoid model improvements. In regards to the geoid modeling procedure, the neglected G1 term will have to be added back to obtain a more accurate geoid model in the mountainous areas, such as the Rocky Mountains. A more accurate geoid to quasigeoid separation term (Table 4) is also needed to transform from the classical orthometric height system into the true orthometric system (Li et al., 2018b). In addition, a more rigorous weighting scheme for the airborne data is desired to fully take advantage of the gravity signal from the GRAV-D data. Finally, for model evaluation, a step-by-step comparison with the NRCan geoid models is needed for the upcoming vertical datum unification. Alternative terrain modeling methods (Wang et al., 2019), recently developed at NGS, will also need to be tested during future experimental geoid model development.

Appendix I: GRAV-D Blocks

GRAV-D Blocks used in the development of the xGEOID19RefB and xGEOID19B model are listed as follows: AN01, AN02, AN03, AN04, AN05, AN06, AN07, AN08, AN09, AS01, AS02, AS04, AS05, AS07, CN01, CN02, CN03, CN04, CN05, CS01, CS02, CS03, CS04, CS05, CS06, CS07, CS08, EN01, EN02, EN03, EN04, EN05, EN06, EN07, EN08, EN09, EN10, ES01, ES02, ES03, ES04, ES05, ES06, ES09, ES10, MS02, MS03, MS04, MS05, PN01, PN02, PS02, and TS01.

Appendix II: Geoid Evaluation with Astrogeodetic Deflections of the Vertical and ICESat-2

Astrogeodetic Observations

NGS possesses over 4,000 observations of astronomical latitude and longitude across North America and its periphery acquired between the 1850s and the 1980s (Strange, 1989). More than half of these observations were performed as part of the Transcontinental Traverse of

CONUS from 1961–1976, which furnished measurements along traverses with 8 km spacing. These measurements were not used to make xGEOID19 and are instead set aside to independently verify geoid slopes. The locations of these observations are shown in Figure A1.

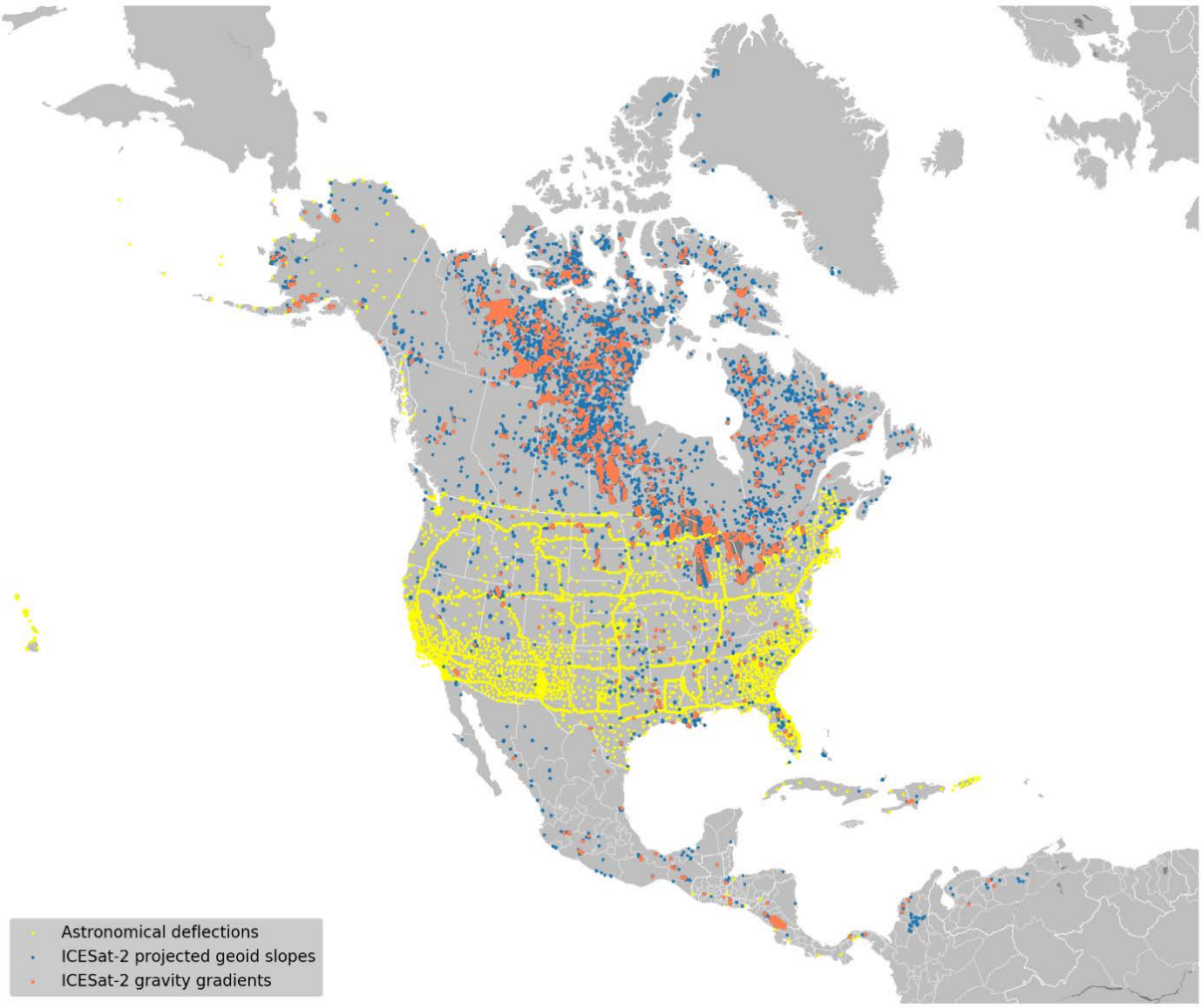

Figure A1: Positions of astronomical deflections of the vertical, water surface slopes measured with ICESat-2, and full paraboloid fits measured with ICESat-2.

Astrogeodetic observations may be contrasted with gravity and GNSS/leveling in that their prime sensitivities are in the horizontal plane, rather than along the plumb line. As such, they are advantageous in rugged terrain because they are relatively insensitive to errors in observation elevation but highly sensitive to local terrain effects. They have therefore been incorporated into geoid models in Switzerland (Marti, 2007) and Austria (Wellenhof and Mortiz, 2006). Astrogeodetic geoids have been developed in the United States by, e.g., Fischer et al (1968) with decimeter precision. Another advantage of these measurements is their relative insensitivity to time variations in geopotential and measurement height. The largest deflection of vertical (DoV) rates predicted by GRACE are on the order of 1 milliarcsecond yr^{-1}, which requires many decades to produce a 1σ error. This may be contrasted with GNSS/leveling, which may be affected by recent elevation change. In Alaska, gravity and elevation changes from ice mass loss and solid-Earth processes may introduce decimeter-scale errors to GNSS/leveling. The

limited extent of Alaska's vertical control network also restricts where GNSS/leveling is available. By contrast, because Alaskan horizontal control is more extensive than its vertical control, 47 complete observations of astronomical latitude and longitude are available across the state with consistent quality and spatial distribution. The tradeoff in sensitivity comes with the caveat that DoV measurements are sensitive to horizontal crustal motion, particularly stemming from earthquakes.

Typical reported measurement errors for these observations were in the range of ±0.1–0.2". The external accuracy of NGS's inventory of astrogeodetic observations was evaluated by Strange (1989) and found to be on the order of 0.2". There are long-wavelength systematic errors of less than 0.1" unique to each observation that reflect polar motion and subtle reference frame differences that could spuriously indicate long-wavelength geoid tilts if the dataset is not spatially band-pass filtered. For a point comparison, these effects are less important.

The available data are given as astronomical latitudes and longitudes, which may be understood as the orientation of the plumb line with respect to Earth's rotation axis and prime meridian. These astronomical coordinates may be differenced with NAD83 geodetic coordinates to obtain deflections of the vertical. To predict deflections of the vertical on a planet with average radius R at latitude ϕ and longitude λ, the xGEOID19 grid was numerically differentiated in the north and south directions with second-order central differences and scaled to match geodetic sign conventions and the local coordinate scale.

$$\eta = -\frac{1}{R\cos\phi}\frac{\partial N}{\partial \lambda}$$

$$\xi = -\frac{1}{R}\frac{\partial N}{\partial \phi}$$

The validation begins by subtracting the predicted deflections from the geoid slopes. Following Wellenhof and Moritz (2006), a plumb line curvature correction was computed for the normal and Bouguer components of the gravity field and propagated up to the altitude of the measurements before comparison. The weighted RMS of the residuals was used as the figure of merit for comparison, with the inverse square of the reported observation uncertainty used as the weight.

Results of this comparison with xGEOID19B are shown in Figure A2 and detailed in Table A1. The effect of GRAV-D on the model errors is illustrated in Figure A2 and detailed in Table A2.

The overall weighted RMS agreement with observed deflections of the vertical is 1.5" in η and 0.8" in ξ across CONUS, implying 1.2" precision in geoid slope for an arbitrary direction. The scale of these residuals is dependent on whether the surrounding terrain is mountainous. Therefore, CONUS is further subdivided into eastern and western zones. The western zone includes all Mountain and Pacific states, or Arizona, California, Colorado, Idaho, Montana, Nevada, New Mexico, Oregon, Utah, Washington, and Wyoming. In these states, the wRMS of the residuals is 2.2" in η and 1.1" in ξ, or 1.7" in an arbitrary direction. The remaining states in the eastern zone display substantially better wRMS agreement, with 0.5" in η and 0.6" in ξ. No statistically significant improvement is evident between xGEOID19A and xGEOID19B in CONUS.

In Alaska, astronomical DoV residuals are largest in the Alaska Range in the southcentral part of the state. This is mostly attributable to the ruggedness of its terrain, but part of the error is because of accumulated horizontal crustal motion following the collection of these observations in the 1940s and 1950s. Horizontal position changes of more than 3 m following the 1964 Prince William Sound earthquake introduce correctable systematic errors on the order of 0.1". The overall scale of the error is comparable to the western part of CONUS, with 2.2" in an arbitrary direction, but the east-west orientation of the Brooks and Wrangell ranges introduces the strongest terrain effects to ξ, whereas the north-south orientation of the Rockies introduces the most terrain signal to η. No statistically significant improvement in the residuals from the introduction of GRAV-D is evident, but corrections to ξ are as large as 1.8".

Puerto Rico exhibits comparably large residuals to other topographically rugged areas (1.3" in η and 1.9" in ξ). Hawaii, where GRAV-D is not yet available, but 26 astrogeodetic observations are, displays large wRMS residuals of over 2" in both directions.

Deflections of the vertical may herald imminent geoid improvement in the western United States. Spatially correlated residuals of more than ±1" are present in the Sierra Nevada range, western Montana, and at the US–Canada border in Washington. GRAV-D data for these regions are being collected as of August 2019.

ICESat-2

Where inland water is sufficiently still, the shape its takes reflects a surface of equal gravitational potential with a shape similar to the geoid. The local slopes of the water surface provides the deflection of the vertical and its curvature provides the horizontal components of the gravity gradient tensor. Satellite altimetry may be used to recover the water surface shape and transform the variations therein to gravity anomalies. This has been exhaustively demonstrated over open ocean. (Sandwell and Smith,1997). Traditionally, these methods perform a spectral transformation of geoid slopes measured by differentiating satellite altimetry along track. Full defections of the vertical were only possible to directly measure at crossover points. These measurements were not normally available over smaller bodies of inland water and could only measure geoid slope along the satellite's ground track.

These limitations are overcome by ICESat-2, launched in 2018 (Abdalati et al., 2010), which provides precise measurements of the geometric surface of inland water in North America. ICESat-2 is unique in that it operates six laser beams simultaneously. The beams are arranged in three cross-track pairs, with each pair about 3.2 km apart, providing instantaneous measurement of water surface height in both the along-track and cross-track directions with a relative height precision of 1-2 cm. This means that a single pass from ICESat-2 over water can recover both components of the deflection of the vertical across a sufficiently long baseline. The baseline provided by the cross-track spacing between beams is sufficient for 0.3" precision in geoid slope measurement.

The starting point for this analysis was the ATLAS/ICESat-2 L3A Inland Water Surface Height, Version 1 product, designated ATL13 (Jasinski and Stoll, 2019). This product was subsetted over North America and a limited number of surrounding territories. All altimetry shots coming from bodies classified as either a lake or a reservoir with a surface area greater than 10 km^2 were isolated. For each ground track, data were placed into bins for every 0.95 seconds

(~6.9 km) of along-track travel. The center of each bin was marked by the most central shot from "GT2R", one of the central two ground tracks in the six-laser ensemble.

To produce gravity gradients from paraboloid fits to water surfaces, the data are windowed to a range of ±3.2 km along track, matching the cross-track spacing of the laser beam pairs. This windows the data into an approximate square with a roughly equal baseline both along- and cross-track. For each window, the data therein are converted to a local east-north-up coordinate system with x representing east deviation from the window center and y representing the north component. To remove sudden discontinuities, the time series of altimetry elevations along each ground track in the window is numerically differentiated and masked where the absolute value of the numerical derivative is greater than 0.1 rad, indicating a discontinuity in the time series. If the remaining data in the window have less than 100 points or less than five individual laser beams, the paraboloid is rejected and the next window is considered.

Otherwise, a paraboloid is fit to the remaining altimetry with the equation

$$h(t,x,y) = h_0(t) - \eta\, x - \xi\, y + \frac{1}{2}\frac{\Gamma_{xx}}{g}x^2 + \frac{1}{2}\frac{\Gamma_{yy}}{g}y^2 + \frac{1}{2}\frac{\Gamma_{xy}}{g}xy$$

where the free parameters are h_0, η, ξ, Γ_{xx}, Γ_{yy}, and Γ_{xy}. This equation is a second-order expansion of the geoid into two-dimensional slopes and curvatures based on one-dimensional relationships described by Sandwell and Smith (1997). The bias term h_0 represents the mean height anomaly in of the water surface in the window. The deflections of the vertical $\eta$and ξ are the partial derivatives of the water surface slope defined with astronomical sign conventions and represent east-west and north-south deflections, respectively. The gravity gradient tensor components, Γ_{xx}, Γ_{yy}, and Γ_{xy} describe the curvature of the water surface observable by the altimeter. Finally, the constant g is the mean value of gravity at Earth's surface.

Once this fit is performed residuals more outlying a 5σ bound are rejected. The remaining data are used to recompute the parameters of interest. The data are further filtered for water surface curvature using the gravity gradients. If the maximum curvature of the water surface is outside the range of what is naturally expected from gravity gradients predicted by topography, then it may be considered to be influenced by hydraulic action and cannot be used to measure an equipotential surface. Hydraulic signals are removed by assembling Γ_{xx}, Γ_{yy}, and Γ_{xy} into a gravity gradient tensor and computing its eigenvalues. If either eigenvalue is more extreme than 180 E (1 E = 10^{-9} s^{-2}), the measurement is rejected. As a final step, the formal errors of the fit are computed with the residuals and covariance matrix. If the error in the deflections of the vertical exceeds 1 arcsecond, the measurement is rejected.

Along-track slopes are also computed for individual ground-tracks. These are advantageous for capturing surface slopes on smaller bodies of water that cannot fit all six ICESat beams at once. The measured along-track slope may be predicted from the geoid by projecting deflections of the vertical along the azimuth of the spacecraft groundtrack.

For each fit center, the data are windowed to a range of ±3.2 km about the fit center along track. As with the gravity gradient solutions, the altimetry data is converted into a local east-north-up frame with x representing east deviation from the window center, y representing the north component, and t being the elapsed time before and after the satellite passes the window

center. The spacecraft velocity within this interval is estimated by a least-squares fit to the beam's horizontal position in time.

$$x = v_x t$$

$$y = v_y t$$

$$v = \sqrt{v_x^2 + v_y^2}$$

The along-track slope ε of the water surface and the mean water surface height h_0 be estimated with the velocity and observed altitude via the equation

$$h(t) = h_0 - \varepsilon v t.$$

The slope is related to the deflection of the vertical components $\eta$and ξ by

$$\varepsilon = \xi \frac{v_y}{v} + \eta \frac{v_x}{v}.$$

The components of the deflection of the vertical cannot be estimated from a single along-track observation, but may be recovered at known crossover points. As with the gravity gradient solutions, the data used to make the along-track slopes are filtered with sigma rejection and the measurement is rejected if the formal error exceeds 1" or if the curvature of the residuals is consistent with a gravity gradient of more than 100 E. Gravity gradient limits must be more stringent in one dimension as gradient tensor eigenvalues are not accessible.

For Version 1 of the ATL13 product, 26,005 along-track slopes and 3,880 complete paraboloids with deflections and gravity gradients were recovered within the analysis domain. The overwhelming majority of these points are in the Canadian subarctic, where the footprint of the former Laurentide ice sheet has left the landscape dotted with thousands of lakes. Over 2,800 recovered gravity gradients and 20,600 along-track slopes are in Canada and Greenland. By contrast, only 194 gradients and 1,505 slopes were measured in CONUS. Alaskan lakes contributed to 81 gradients and 460 slopes. The Great Lakes provided 580 gradients and 2,362 along-track slopes. Additional altimetry was captured in Mexico, Central America, and the Caribbean. Typical formal errors for the deflections of the vertical obtained in the gradient fits were ±0.1–0.3" (0.5–1.5 mm km^{-1}). Despite reduced data and shorter baselines, the along-track slopes give similar performance. Compare with historical astronomical measurements with 0.1-0.2" reported precision.

Some caveats are included with this dataset. First, ICESat-2 cross-track slopes are not yet fully calibrated (Scott Luthcke, personal communication) and therefore cross-track deflections may be affected by inter-laser bias. This adds random offsets to the η component of the deflection of the vertical. Setup effects from winds and currents may also affect the data, particularly in the Great Lakes. As prevailing winds are in the east-west direction, the η of the deflection of the vertical is most sensitive to these errors. Wind-driven setup is inversely proportional to the average depth of the lake (Bennett, 1974), so more caution is required around shallower lakes. An error source unique to the Great Salt Lake is the hydraulic partition introduced by a railroad berm bisecting the lake. Poor hydraulic communication between the two halves of this lake introduces a ~20 cm discontinuity in surface height across this boundary. Finally, these kinds of observations are only possible where the topography and climate of a

region are amendable to the formation and persistence of lakes. Therefore, these kinds of observations may not statistically represent rugged terrain as well as terrestrial astrogeodetic observations.

These data were compared with deflections computed from the east-west and north-south gradients of xGEOID19 A and B. The overall model agreement with the data is shown alongside astrogeodetic results in Table A1 and the corresponding Figure A2. The effect of GRAV-D is evaluated in Figure A3 and Table A2. Across CONUS, weighted RMS agreement with ICESat-2 inland water surface slopes is 1.8" for η, 0.7" in ξ, and 1.1" along track with no apparent improvement between model A and B. Overall agreement is in Alaska is 1.5" in η, 1.1" in $\xi$and 1.1" along-track with no improvement evident between models.

Altimetry over the Great Lakes does show statistically significant improvement in geoid slope and deflection of the vertical where GRAV-D data were introduced. Here, xGEOID19A and xGEOID19B show wRMS agreement of 1.6" in η, but xGEOID19A's residual error is 0.75" vs. xGEOID19B's 0.66". Along-track measurements show a similar 0.9" wRMS between the two models, with a reduction in wRMS of from 0.91" in model A to 0.86" in model B. An F-test indicates p-values of 0.0011 for the differences in ξ and 0.003 for along-track slope. Bartlett and Levene statistical tests provide a less optimistic interpretation, with p values of ~0.3.

ICESat-2, with microradian-precision in both along-track and cross-track measurements, provides a novel approach to geoid validation and measurement. This mission highlights improvement in the accuracy the geoid from the addition of GRAV-D data. The use of ICESat-2 for geoid validation will evolve as additional ICESat-2 cycles become available and cross-track biases between beams become manageable.

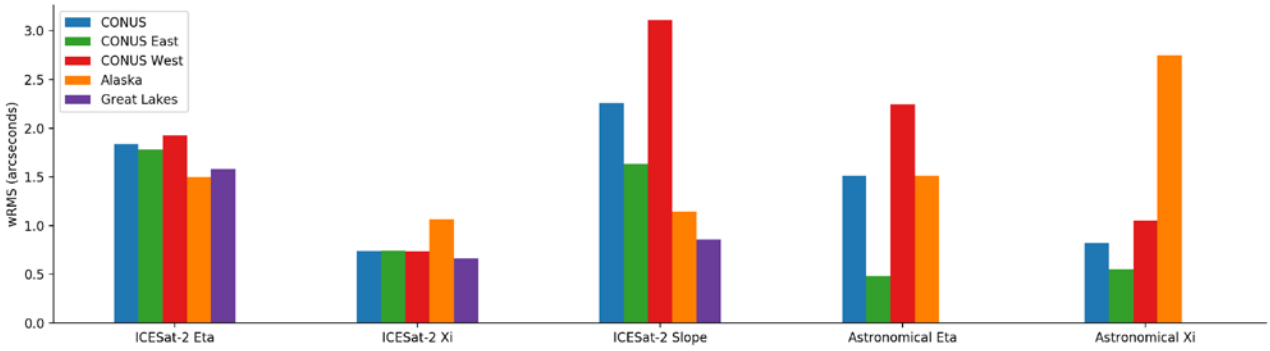

Figure A2: Regional evaluation of the weighted RMS of the residuals of xGEOID19B against ICESat-2 and astrogeodetic techniques

Table A1: Performance of xGEOID19B deflection of the vertical and geoid slopes compared with ICESat-2 and astronomical deflections

Weighted RMSE (arcseconds)	**CONUS**	**CONUS East**	**CONUS West**	**Alaska**	**Great Lakes**
ICESat-2 η	1.83	1.78	1.92	1.50	1.57
ICESat-2 ξ	0.73	0.74	0.73	1.06	0.66
ICESat-2 ε	2.25	1.63	3.1	1.14	0.85
Astronomical η	1.50	0.48	2.2	1.51	–
Astronomical ξ	0.82	0.55	1.05	2.7	–

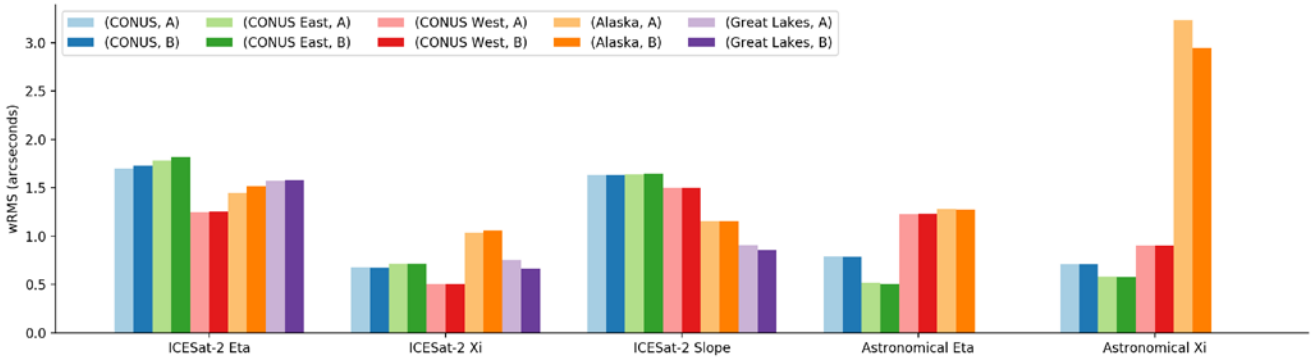

Figure A3: Regional evaluation of the effect of GRAV-D between xGEOID19A (pastel shades) and xGEOID19B (dark shades) geoid slopes and deflections of the vertical measured by ICESat-2 and astrogeodetic techniques. Only data points within regions where GRAV-D data were collected are considered.

Table A2: Performance of xGEOID19 A and B deflections of the vertical and geoid slopes compared with ICESat-2 and astronomical deflections in areas where GRAV-D contributed new airborne gravity data. Statistically significant improvement is highlighted with an asterisk.

Weighted RMSE (arcseconds)	**CONUS**		**CONUS East**		**CONUS West**		**Alaska**		**Great Lakes**	
Model	**A**	**B**	**A**	**B**	**A**	**B**	**A**	**B**	**A**	**B**
ICESat-2 η	1.70	1.72	1.78	1.81	1.25	1.25	1.44	1.51	1.57	1.58
ICESat-2 ξ	0.68	0.68	0.71	0.71	0.50	0.50	1.03	1.06	0.75*	0.66*
ICESat-2 ε	1.63	1.64	1.64	1.64	1.50	1.50	1.15	1.16	0.91*	0.86*
Astronomical η	0.79	0.79	0.51	0.50	1.22	1.23	1.28	1.27	–	–
Astronomical ξ	0.71	0.71	0.58	0.58	0.90	0.90	3.23	2.94	–	–

References

Abdalati, W., Zwally, H. J., Bindschadler, R., Csatho, B., Farrell, S. L., Fricker, H. A., Harding, D. et al. (2010). The ICESat-2 laser altimetry mission. Proceedings of the IEEE, 98(5): 735-751.

Ahlgren, K., Wang, Y.M., Li, X., and Youngman, M. (2018). Towards a More Consistent Geoid Model for North America. FIG Congress 2018 Proceedings, Istanbul, Turkey.

Andersen, O.B., Stenseng, L., Piccioni, G., & Knudsen, P. (2016). The DTU15 MSS (Mean Sea Surface) and DTU15LAT (Lowest Astronomical Tide) reference surface. ESA Living Planet Symposium 2016, Prague, Czech Republic.

Barnes, D.F. (1976). Bouguer gravity map of Alaska: U.S. Geological Survey Open-File Report 76-70, 1 sheet, scale 1:2,500,000.

Bennett, J.R. (1974). On the Dynamics of Wind-Driven Lake Currents. J. Phys. Oceanogr. 4: 400–414. https://doi.org/10.1175/1520-0485(1974)004<0400:OTDOWD>2.0.CO;2

Fischer, I., Slutsky, M., Shirley, F.R. et al. (1968). New pieces in the picture puzzle of an astrogeodetic geoid map of the world. Bull. Geodesique 88: 199. https://doi.org/10.1007/BF02525661

Forsberg, R. (1984). A study of terrain reductions, density anomalies and geophysical inversion methods in gravity field modeling. The Ohio State University, OSU report no. 355, Columbus, OH, USA.

Beckley, B., Ray, R., Holmes, S., Zelensky, N., Lemoine, F., Yang, X., Brown, S., Desai, S., Mitchum, G., and Hausman, J. (2013). Integrated multi-mission ocean altimeter data for climate research complete time series version 2. Available from ftp://podaac.jpl.nasa.gov/allData/merged_alt/preview/L2/docs/multi_alt_handbook_v2.p df.

Howat, I.M., Negrete, A., Smith, B.E. (2014). The Greenland Ice Mapping Project (GIMP) land classification and surface elevation datasets, The Cryosphere, 8, 1509-1518, doi:10.5194/tc-8-1509-2014

Huang, J., Véronneau, M. (2013). Canadian gravimetric geoid model 2010. J. Geod. 87: 771-790.

Jarvis, A., Reuter, H.I., Nelson, A., Guevara, E. (2008). Hole-filled SRTM for the globe Version 4. Available from the CGIAR-CSI SRTM 90m Database (http://srtm.csi.cgiar.org).

Jasinski, M. F., and Stoll, J.D. (2019). ATLAS/ICESat-2 L3A Inland Water Surface Height, Version 1. Boulder, Colorado USA. NASA National Snow and Ice Data Center Distributed Active Archive Center. https://doi.org/10.5067/ATLAS/ATL13.001. [2019-06-03].

Jacob, T., Wahr, J., Gross, R., Swenson, S., and Geruo, A. (2012). Estimating geoid height change in North America: past, present and future. J. Geod. *86*(5): 337-358.

Krcmaric, J.A., Wang, Y.M., Li, X., Ahlgren, K. (2019). Propagation of error in geoid computations by the Monte Carlo method. 27th IUGG General Assembly, July 8-18, Montreal, Canada.

Li, X., Roman, D.R., Wang, Y.M., Saleh, J. (2008) High Resolution DEM over Alaska and Its Application to Geoid Modeling. AGU Fall Meeting 2008, San Francisco, CA, USA.

Li, X., Crowley, J.W., Holmes, S.A., Wang, Y.M. (2016). The contribution of the GRAV-D airborne gravity to geoid determination in the Great Lakes region. Geophys. Res. Lett. 43, 4358–4365, doi:10.1002/2016GL068374

Li, X., Huang, J., Wang, Y.M. (2018a). Discussions on the Downward Continuation of Airborne Gravity Data and its Combination with Surface Gravity Data for Local Geoid Modeling. GGHS 2nd Joint Meeting 2018, Copenhagen, Denmark.

Li, X and Wang, Y.M. (2018b). Discussion of the Geoid to Quasigeoid Separation and its Relationship to Leveled Heights a case study in Colorado with a full extension to CONUS. AGU Fall Meeting 2018, Washington, D.C., USA.

Marti, U. (2007). Comparison of High Precision Geoid Models in Switzerland. Dynamic Planet. Springer, Berlin. doi:10.1007/978-3-540-49350-1_55

NGA (2008). Gravity Station Data Format and Gravity Anomalies. Office of GEOINT Sciences. 1 October 2008.

Pavlis, N.K., Holmes, S.A., Kenyon, S.C., and Factor, J.K. (2012). The Development and Evaluation of the Earth Gravitational Model 2008 (EGM2008). J. Geophys. Res. 117: 1-38.

Saltus, R.W., Brown, P.J. II, Morin, R.L., and Hill, P.L. (2008). 2006 compilation of Alaska gravity data and historical reports: U.S. Geological Survey Digital Series 264. CD-ROM.

Sandwell, D. T., & Smith, W. H. (1997). Marine gravity anomaly from Geosat and ERS 1 satellite altimetry. *J. Geophys. Res. 102*(B5): 10039-10054.

Smith, D.A., Holmes, S.A., Li, X., Guillaume, S., Wang, Y.M., Bürki, B., Roman, D.R., and Damiani, T. (2013). Confirming regional 1 cm differential geoid accuracy from airborne gravimetry: the Geoid Slope Validation Survey of 2011. J. Geod. 87: 885-907.

Snay, R. A., Freymueller, J. T., Craymer, M. R., Pearson, C. F., and Saleh, J. (2016). Modeling 3-D crustal velocities in the United States and Canada. J. Geophys. Res. 121: 5365–5388. doi:10.1002/2016JB012884

Strange, W. E. (1989). Extraterrestrial Data. In *North American Datum of 1983.* NOAA Professional Paper NOS 2, pp. 39-46. Rockville, MD. National Geodetic Survey.

Wang Y.M., Saleh, J., Li, X., and Roman, D. R. (2012) The US Gravimetric Geoid of 2009 (USGG2009): model development and evaluation. J. Geod. 86: 165-180. doi: 10.1007/s00190-011-0506-7

Wang, Y.M., Becker, C., Mader, G. et al. (2017). The Geoid Slope Validation Survey 2014 and GRAV-D airborne gravity enhanced geoid comparison results in Iowa. J. Geod. 91: 1261. https://doi.org/10.1007/s00190-017-1022-1

Wang, Y.M., Li, X., Ahlgren, K., and Krcmaric, J. (2019). Results of Colorado geoid computation in NGS. 27th IUGG General Assembly, July 8-18, Montreal, Canada.

Wellenhof, B.H., and Moritz, H. (2006). Physical geodesy. Springer Science & Business Media.

Wong, L., and Gore, R. (1969). Accuracy of Geoid Heights from Modified Stokes Kernels. Geophys. J. R. Astron. Soc. 18: 81-91. https://doi.org/10.1111/j.1365-246X.1969.tb00264.x

Yamazaki D., Ikeshima, D., Tawatari, R., Yamaguchi, T., et al. (2017). A high accuracy map of global terrain elevations. Geophys. Res. Let., 44: 5844-5853. doi: 10.1002/2017GL072874

Zilkoski, D., Richards, J, and Young, G. (1992). Results of the general adjustment of the North American vertical datum of 1988. Surv. Land Inf. Syst., 52(3): 133.

Figures

Figure 1. Data density of terrestrial gravity anomalies used in xGEOID19.

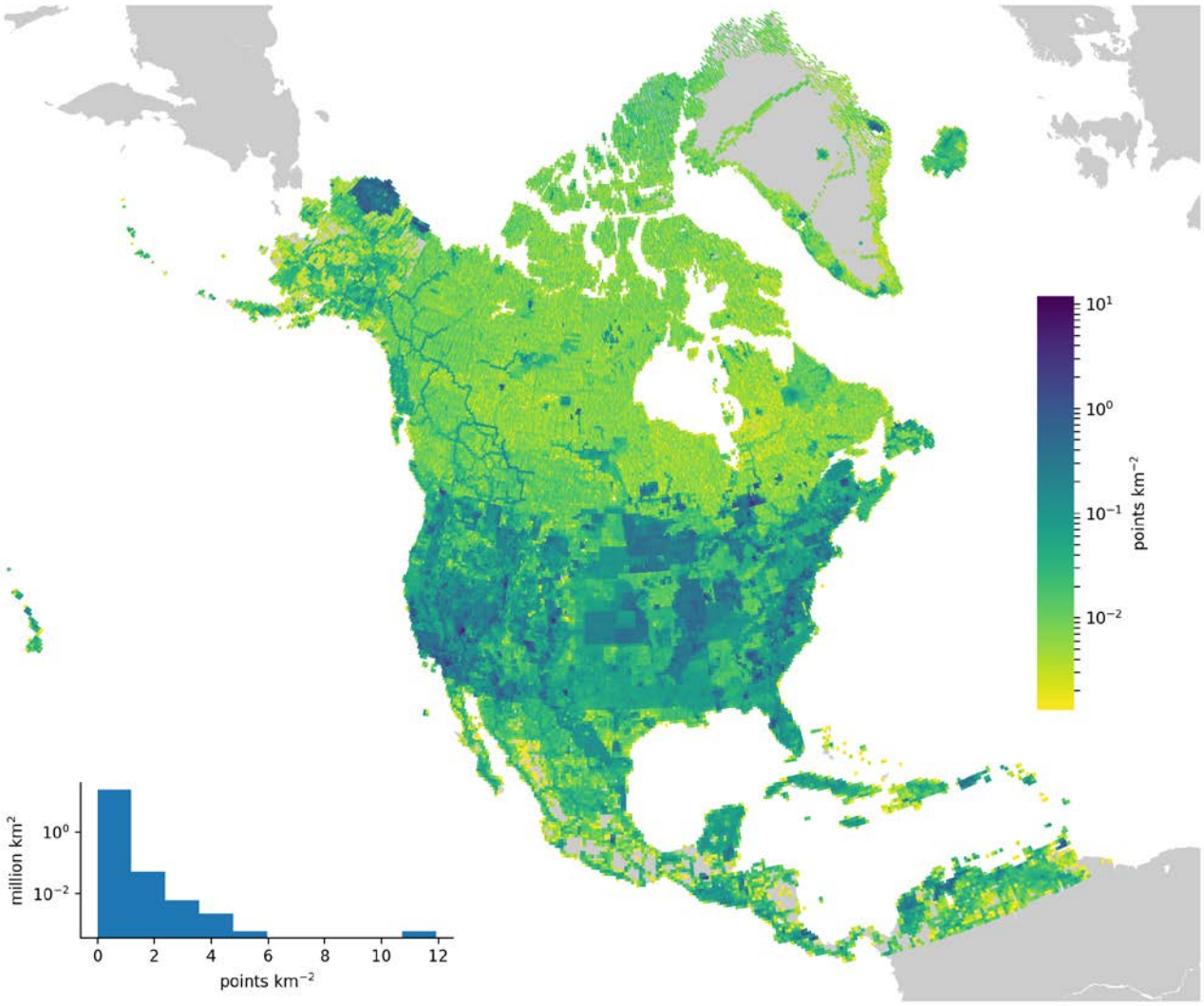

Figure 2. Surface gravity data with source agency.

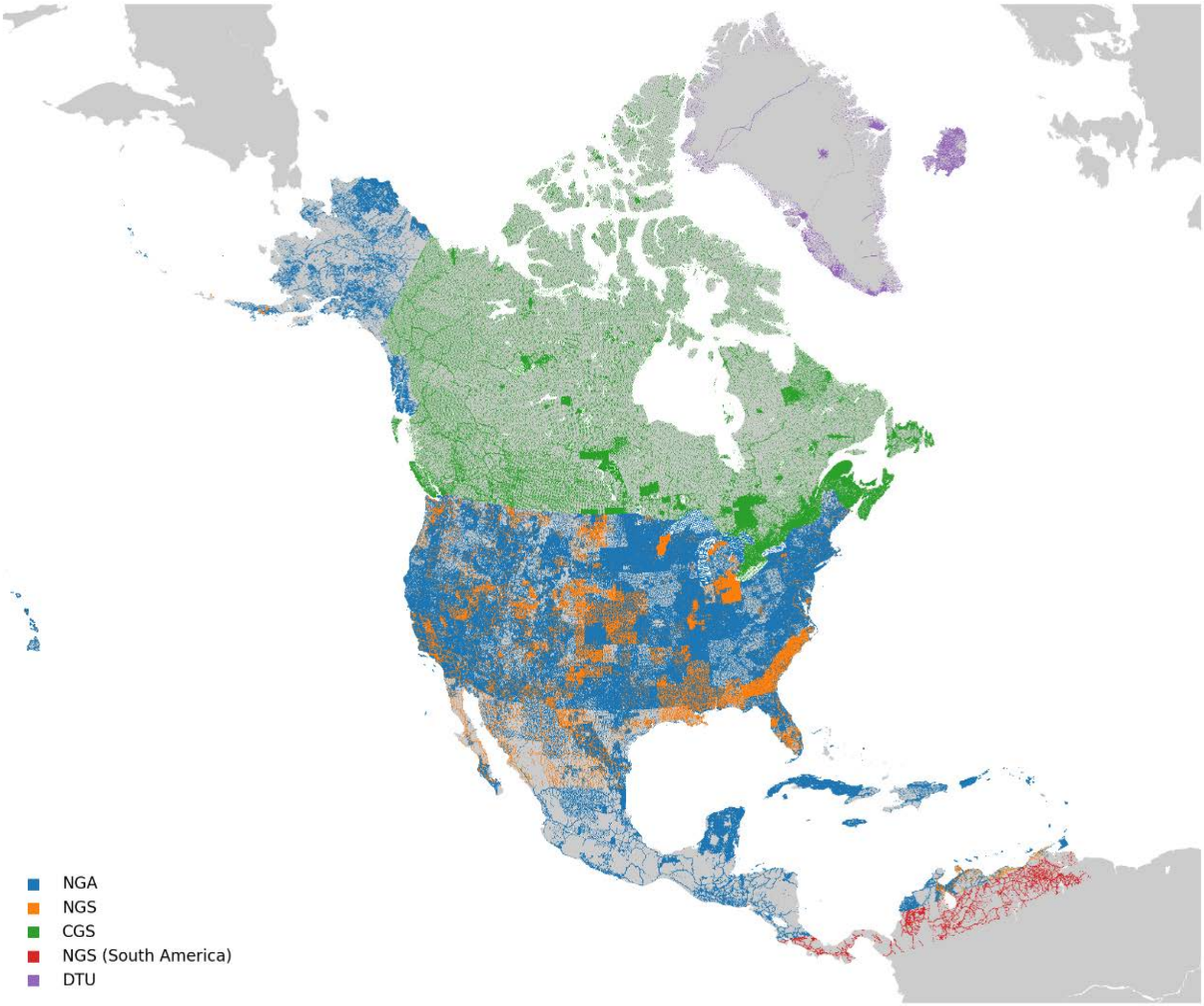

Figure 3. Terrestrial gravity data sources within CONUS.

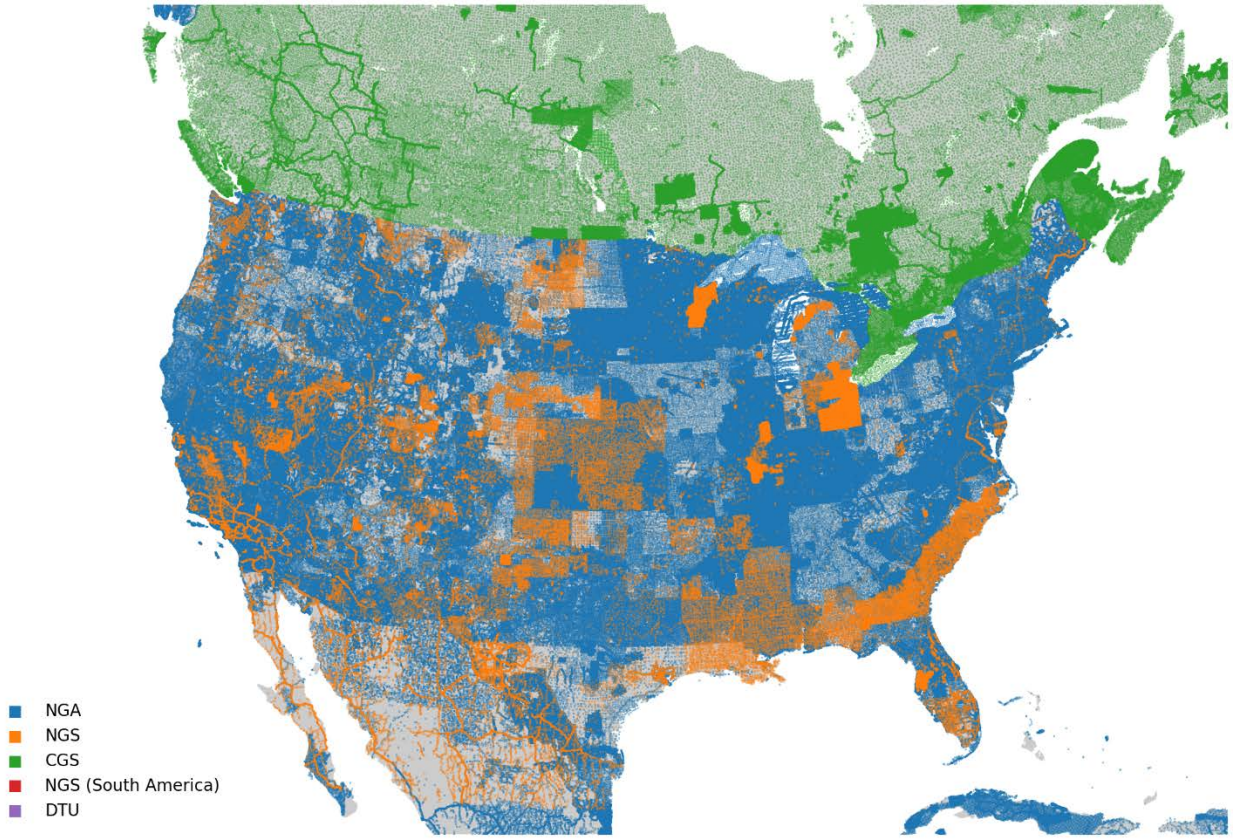

Figure 4: DTU15 gravity anomalies over the open seas around the modeling area.

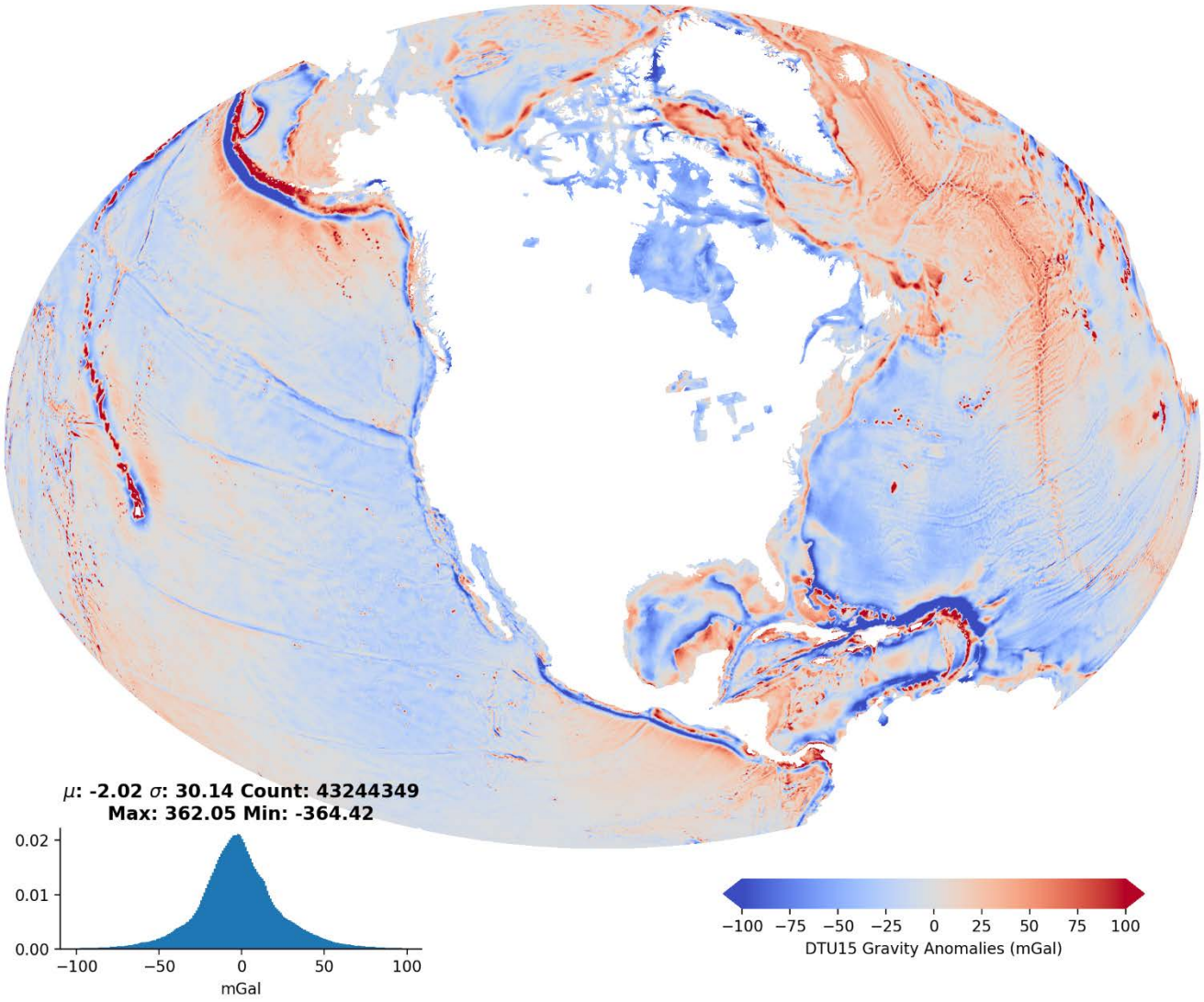

Figure 5: Detected artifacts and the corresponding fixing result in the area of 2°N, 77°W from Ahlgren, et al., 2018. Original DEM (top left), 2 km buffer (top right), Extraction of cells to fill (lower left), Biharmonic Spline Interpolation (lower right).

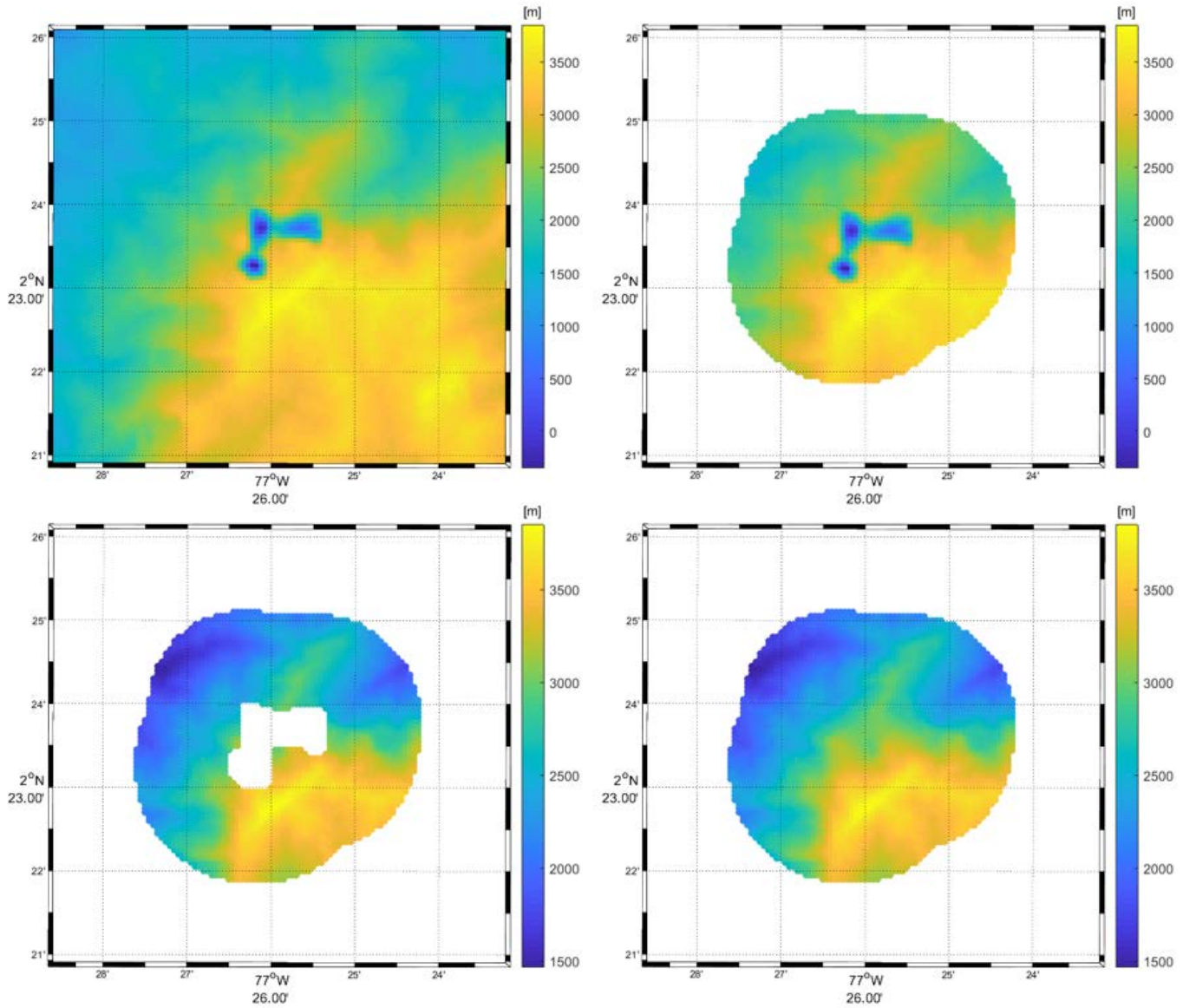

Figure 6: Residual gravity anomalies in the land area.

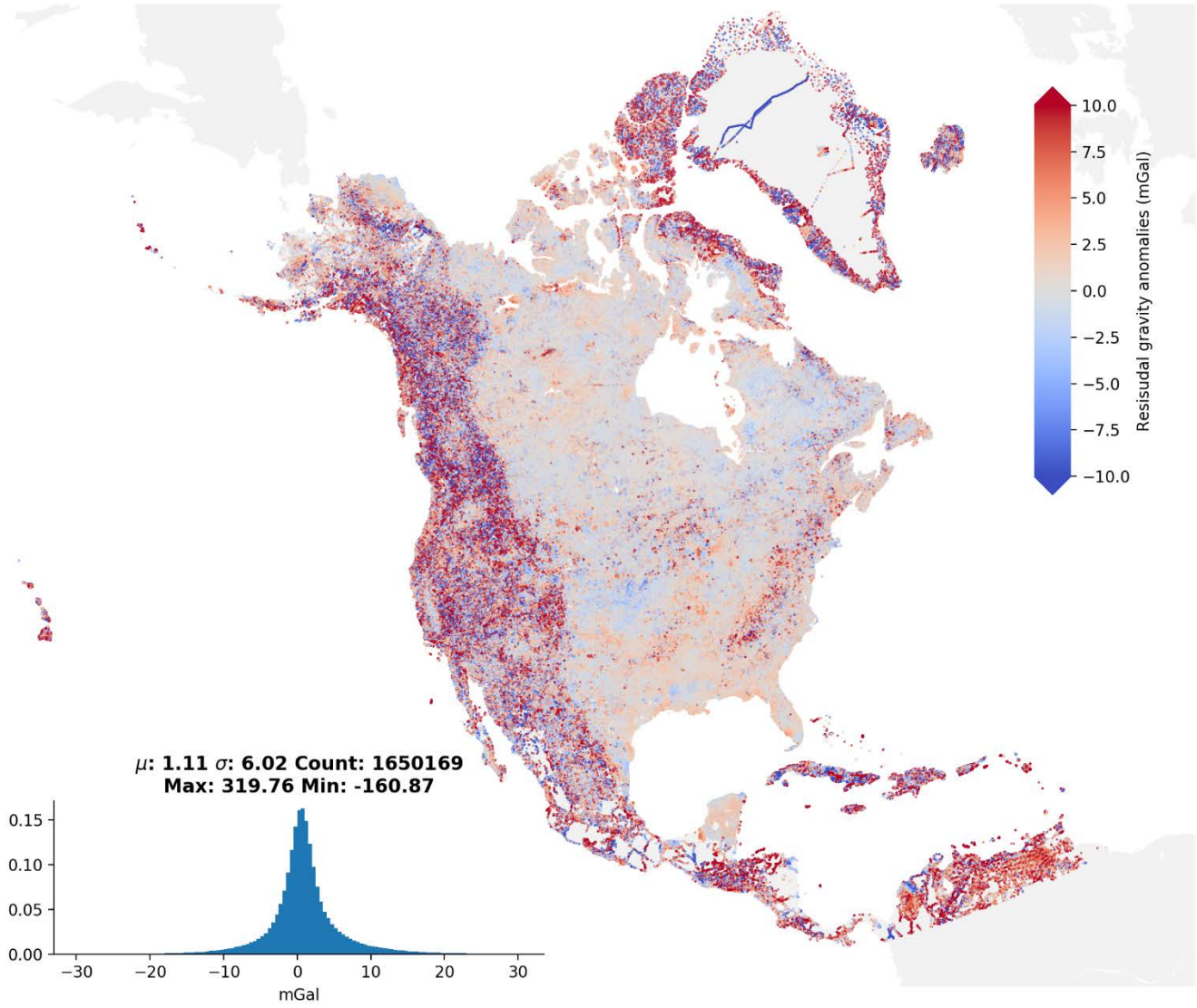

Figure 7: The local gravity and topographic contribution to xGEOID19A.

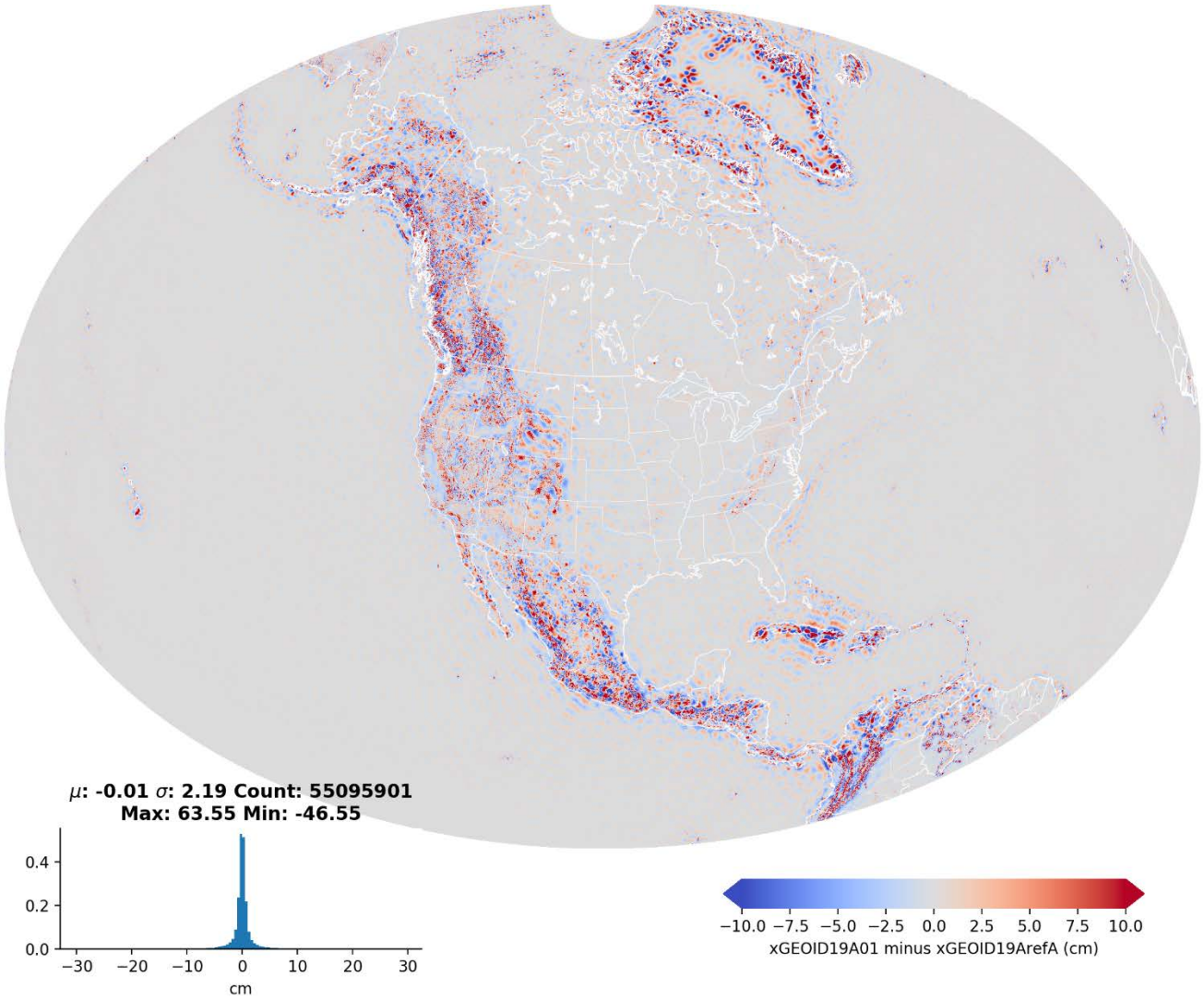

Figure 8. Effects of GRAV-D airborne gravity data on xGEOID19.

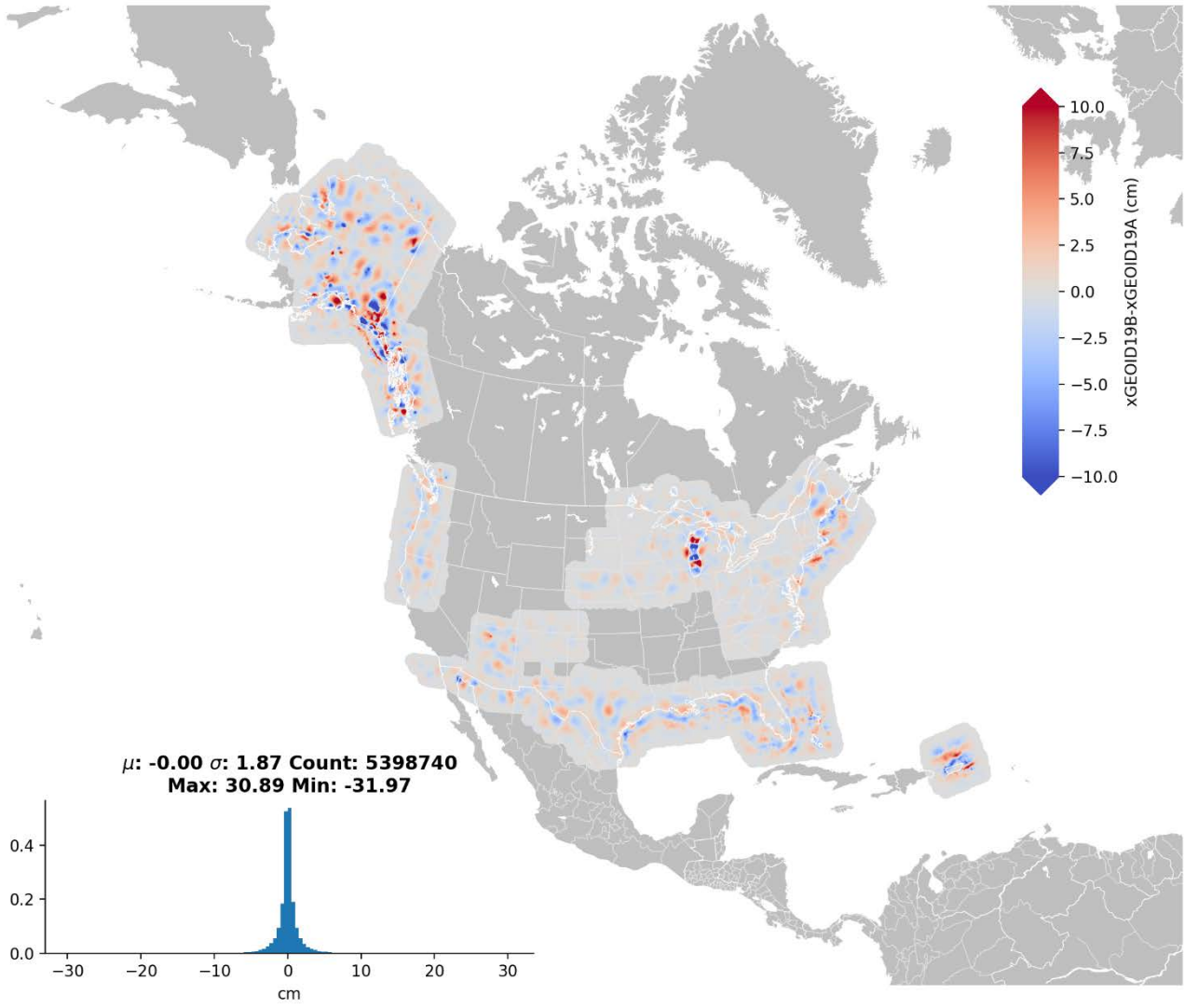

Figure 9. State-by-state height anomaly comparison of the developed reference models for xGEOID19 (with (B) and without (A) GRAV-D gravity data).

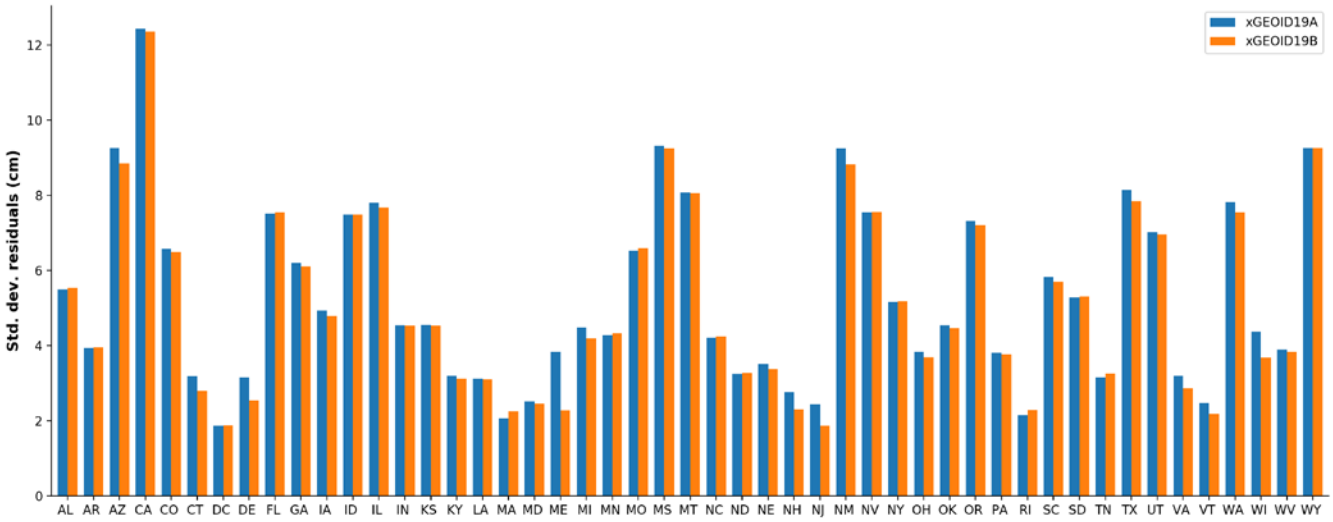

Figure 10. The dynamic height variations computed from the models on the assumed constant heights over the Great Lakes.

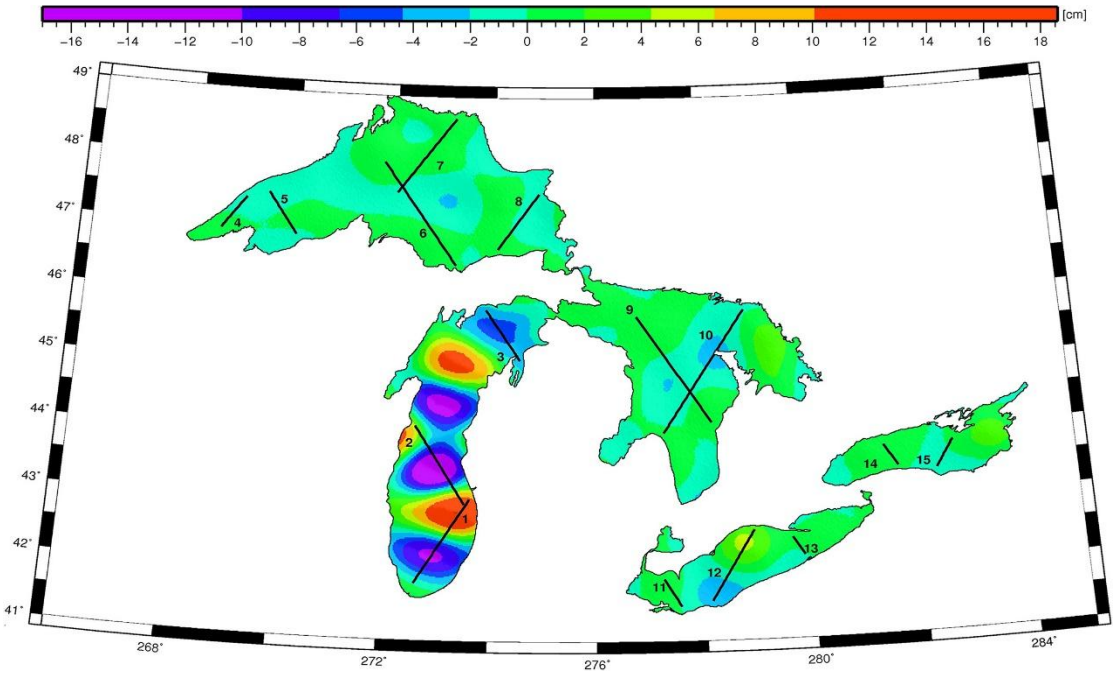

(a) Location of the passes.

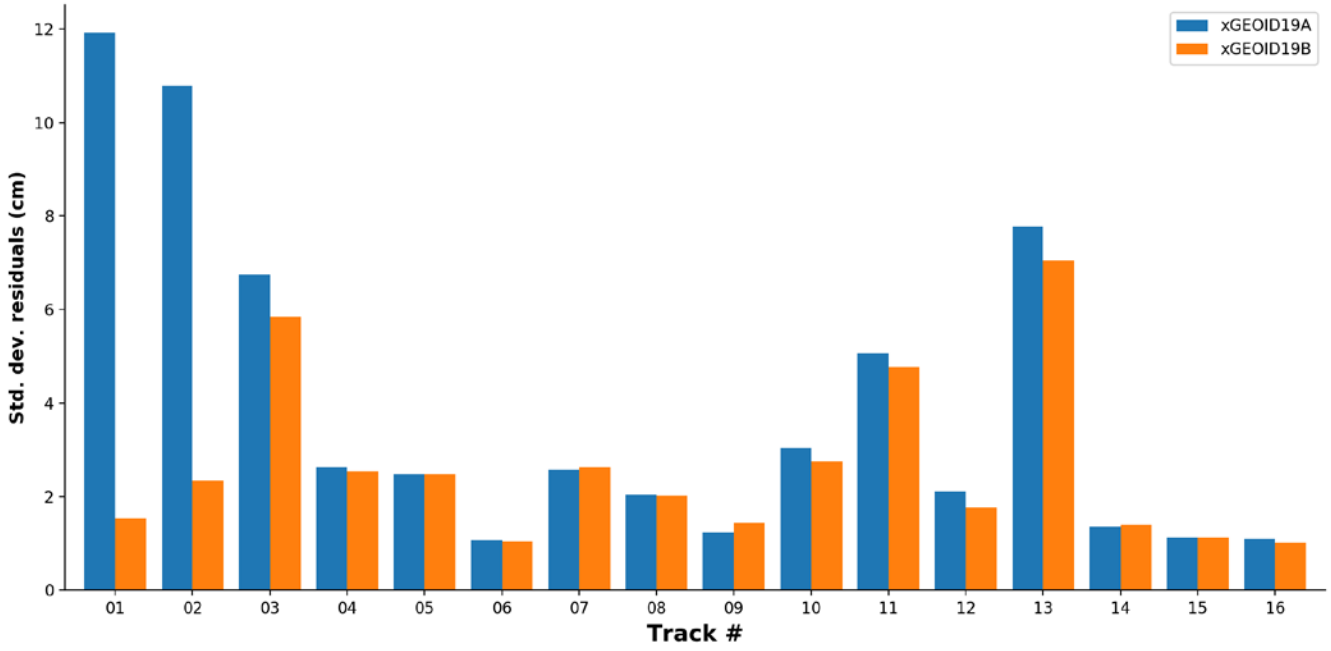

(b) Precision comparisons before and after adding GRAV-D data.

Figure A1: Positions of astronomical deflections of the vertical, water surface slopes measured with ICESat-2, and full paraboloid fits measured with ICESat-2.

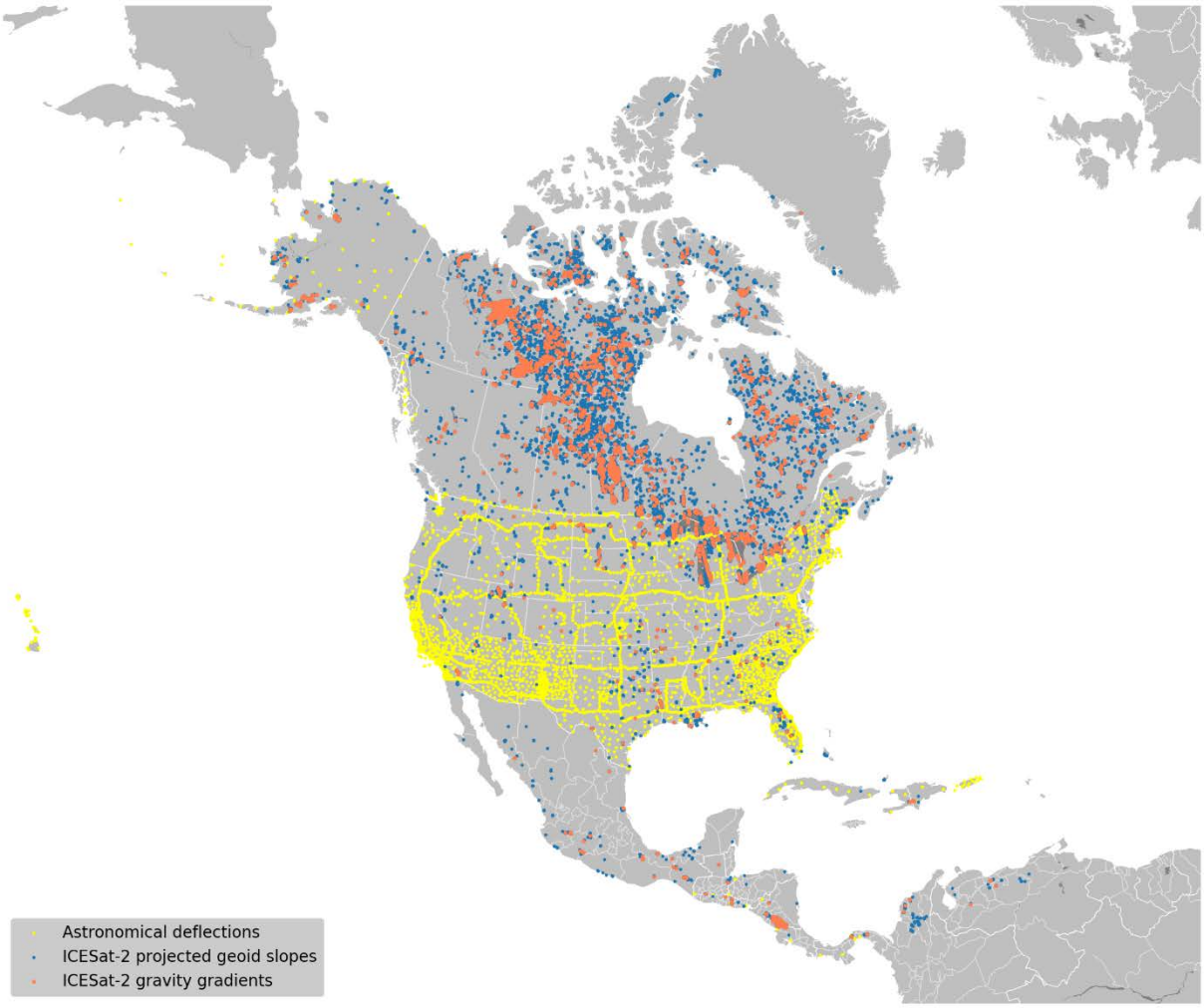

Figure A2: Regional evaluation of the weighted RMS of the residuals of xGEOID19B against ICESat-2 and astrogeodetic techniques

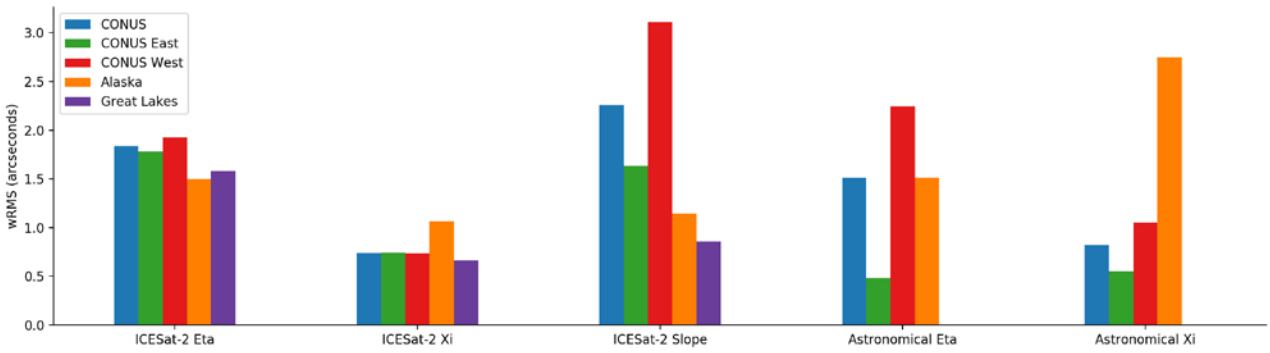

Figure A3: Regional evaluation of the effect of GRAV-D between xGEOID19A (pastel shades) and xGEOID19B (dark shades) geoid slopes and deflections of the vertical measured by ICESat-2 and astrogeodetic techniques. Only data points within regions where GRAV-D data were collected are considered.

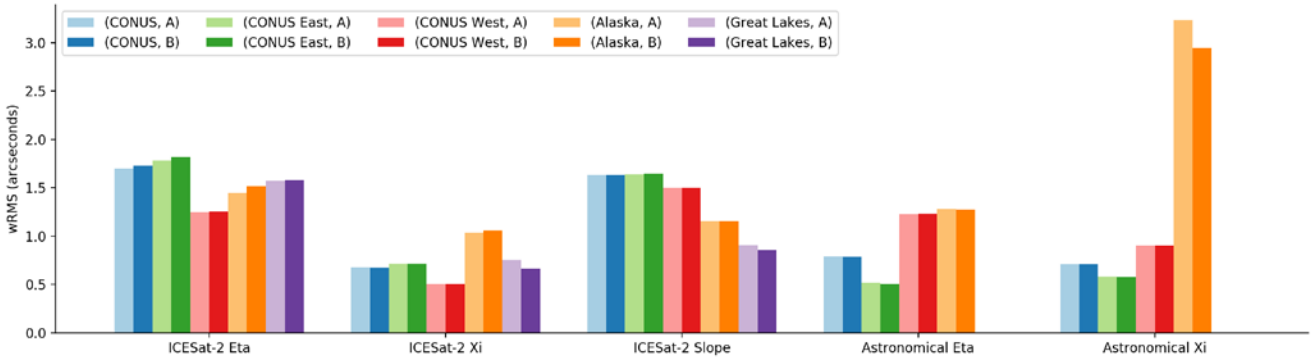

Tables:

Table 1: Input Gravity data to North American common gravity dataset.

	Geographic Region:	Total Number of Points:	Comments:
1	CONUS, Hawaii, Alaska excluding the Great Lakes	1,222,973	NGA data (1,138,596) / NGS data (84,377)
2	Lake Huron, Lake Ontario, and Lake Superior	17,563	NGA data (17,543) / NGS data (20)
3	Lake Michigan	3,151	Data has been cleaned due to known issues (Li, et al., 2016)
4	Canada and Lake Erie	251,313	NRCan-CGS data
5	Caribbean Islands	18,373	NGA data
6	Mexico and Central America	106,210	NGA data
7	South America	15,121	Supplemental data from 7 – 10 degrees from NGS
8	Greenland and Iceland	15,465	DTU data

Table 2: Statistics of the gravity anomalies and each reduction term as well as the final residuals.

(mGal)	Mean	Std	Min	Max
Δg^{OBS}	-3.8	33.7	-309.7	691.1

Δg^{ATM}	0.8	0.1	0.47	0.9
$\Delta g^{OBS} + \Delta g^{ATM} - \Delta g^{REF}_{2\rightarrow 2160}$	-1.9	11.1	-313.3	319.2
$\Delta g^{OBS} + \Delta g^{ATM} - \Delta g^{REF}_{2\rightarrow 2160} - \Delta g^{RTM}_{2161\rightarrow 3''}$	1.1	6.0	-160.9	319.8

Table 3: xGEOID19 model evaluation along GSVS11 and GSVS14 lines.

Standard Deviation (cm)	**xGEOID19A**	**xGEOID19B**
GSVS11 (n = 210)	1.469	0.978
GSVS14 (n = 204)	1.405	1.161

Table 4: Summary of the geoid to quasi geoid omission error tests in **194** historical Benchmarks.

(cm)	**EGM2008 {Cnm Snm}**		**Without GRAV-D {Cnm Snm}**		**With GRAV-D {Cnm Snm}**	
	$\Delta N^{5'}$	$\Delta N^{1'}$	$\Delta N^{5'}$	$\Delta N^{1'}$	$\Delta N^{5'}$	$\Delta N^{1'}$
	8.2	**5.559**	**7.515**	**5.193**	**7.686**	**4.801**

Table 5: Performance of xGEOID19B deflection of the vertical and geoid slopes compared with ICESat-2 and astronomical deflections

Weighted RMSE (arcseconds)	**CONUS**	**CONUS East**	**CONUS West**	**Alaska**	**Great Lakes**
ICESat-2 η	1.83	1.78	1.92	1.50	1.57
ICESat-2 ξ	0.73	0.74	0.73	1.06	0.66
ICESat-2 ε	2.25	1.63	3.1	1.14	0.85
Astronomical η	1.50	0.48	2.2	1.51	–
Astronomical ξ	0.82	0.55	1.05	2.7	–

Table 6: Performance of xGEOID19 A and B deflections of the vertical and geoid slopes compared with ICESat-2 and astronomical deflections in areas where GRAV-D contributed new airborne gravity data. Statistically significant improvement is highlighted with an asterisk.

Weighted RMSE (arcseconds)	**CONUS**		**CONUS East**		**CONUS West**		**Alaska**		**Great Lakes**	
Model	**A**	**B**	**A**	**B**	**A**	**B**	**A**	**B**	**A**	**B**
ICESat-2 η	1.70	1.72	1.78	1.81	1.25	1.25	1.44	1.51	1.57	1.58
ICESat-2 ξ	0.68	0.68	0.71	0.71	0.50	0.50	1.03	1.06	0.75*	0.66*
ICESat-2 ε	1.63	1.64	1.64	1.64	1.50	1.50	1.15	1.16	0.91*	0.86*
Astronomical η	0.79	0.79	0.51	0.50	1.22	1.23	1.28	1.27	–	–
Astronomical ξ	0.71	0.71	0.58	0.58	0.90	0.90	3.23	2.94	–	–